E.T.S. de Ingeniería Industrial,
Informática y de Telecomunicación

Design of THz Metasurfaces for Thin-film sensing

Máster Universitario en
Ingeniería de Telecomunicación

Trabajo Fin de Máster

Irati Jáuregui López

Miguel Beruete Díaz

Pamplona, 20/09/2018

upna Universidad Pública de Navarra
Nafarroako Unibertsitate Publikoa

Acknowledgements

First, I would like to express my gratitude to Dr. Miguel Beruete for constant and excellent guidance (both on a personal and scientific level).

Over the years, the family you choose are those with whom you share joys and sorrows.

To all these good friends, thank you for being there every time I´ve needed you, and for bringing joy in the hard days.

And last but not least, my family. I feel very proud to have the family that I have, and I would like to thank them for their constant love and support and for encouraging me during every difficult moment. Without them none of this would have been possible.

“The universe won´t be great if it weren´t the home of the people you love”
Stephen Hawkings

Abstract

The proposed work is about the design of metasurfaces to work as sensing devices in the terahertz band, for the detection of very thin films. Firstly, a deep simulation study of the behavior of some metasurfaces and its performance as sensors, using the commercial software CST Microwave Studio has been performed. Two kind of structures have been studied: a labyrinth shaped metasurface with an intricate geometry, and two different hole array metasurfaces with different substrate thicknesses, in order to control de appearance of the anomalous extraordinary optical transmission (EOT) resonance, and make a comparison between the regular and the anomalous EOT. Parametric studies have been carried out varying the film thickness deposited on each structure. After an initial statistical analysis, an experimental study has been carried out, showing a good agreement with the numerical results. These results demonstrate the excellent performance of these kind of structures in practical thin-film sensing platforms, improving the results found in the literature.

Resumen

El trabajo propuesto trata sobre el diseño de metasuperficies en la banda de los terahercios para su uso como sensores de películas muy delgadas. En primer lugar, se ha llevado a cabo un estudio profundo de simulación de varias metasuperficies y de su actuación como sensores, mediante el software comercial CST Microwave Studio. Se han estudiado dos tipos de estructuras: una metasuperficie “laberinto”, con una compleja geometría, y dos “hole arrays” con distintos grosores de substrato, con el objetivo de controlar la aparición de la resonancia correspondiente a la transmisión óptica extraordinaria (EOT), y hacer una comparación entre la EOT regular y la anómala. Se ha llevado a cabo un estudio paramétrico variando el grosor de la película depositada en cada estructura. Una vez realizado el estudio estadístico, se ha procedido a realizar un estudio experimental, que muestra un buen acuerdo con los resultados de simulación. Estos resultados demuestran la excelente actuación de este tipo de estructuras en el sensado de películas delgadas, mejorando los resultados presentes en la literatura.

Keywords

Metasurface; sensing; thin-film; terahertz; anomalous EOT

Table of Contents

Chapter 1 3

Introduction and state of the art 3

1.1. The THz band 3

1.2. Thin-film sensing at THz 5

1.3. Metamaterials and Metasurfaces for sensing purposes 8

1.4. Extraordinary Optical Transmission (EOT) 14

1.5. Outline 18

Chapter 2 19

Methodology 19

2.1. Numerical simulator: CST Microwave Studio® 19

2.2. Experimental measurements: ABmm VNA analyzer 21

2.3. Fabrication techniques 25

Chapter 3 28

THz metasurfaces sensors 28

3.1. Labyrinth structures 28

3.2. Hole array structures. EOT 48

Conclusions and future work 58

Conclusions 58

Future work 60

References 61

Author Merits 70

Chapter 1

Introduction and state of the art

1.1. The THz band

The Terahertz (THz) band is the region of the electromagnetic spectrum that lies between microwaves and mid-infrared (MIR), and marks the separation between electronics and photonics, as shown in Figure 1.1(a). The exact boundaries still generate controversy according to the different fields of study, but following the classical band definition of microwaves, the THz range falls between 0.1 and 10 THz, or from 3 mm to 30 μm if we talk in terms of wavelengths.

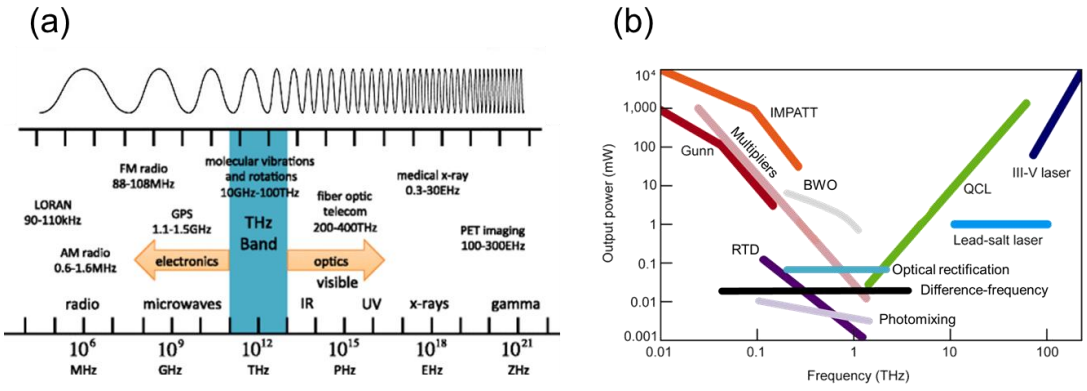

Figure 1.1.. (a) Location of the THz band in the electromagnetic spectrum. (b) The problem of generation. Power-frequency graphs of different sources in the THz band [M. Navarro´s personal communication].

However, this band has not been as studied as other regions in the electromagnetic spectrum and has been historically referred to as the "THz gap", due to

the lack of efficient generators and detectors at this range and the typically high loss of materials at these frequencies. Indeed, due to the fact that we are working at these frequencies the metallic parts of the structures must be modelled as metal with lower electric conductivity than that used in bulky metals. This is due to the roughness of the metal. At other frequencies such as microwaves this is not a worrying fact, since the wavelength is much greater than the average roughness, and the wave does not see it. However, in the THz band the average roughness is comparable to the wavelength, so is necessary to model this fact by reducing the conductivity of the metal with respect to its low frequency value.

Unlike radiation at higher frequencies such as infrared, or at lower frequencies such as microwaves that are easy to generate and detect, THz waves generation and detection is complex due to the fact that the detectors have low sensitivity and in some cases need to work at cryogenic temperatures by the use of liquid helium. Furthermore, the classical sources for both microwave and infrared suffer an important power decrease leading to this technological "gap", as shown in Figure 1.1(b).

Along the years, new generation techniques have been proposed, the great majority of them based on frequency conversion, using Schottky diodes [1], or near-infrared (NIR) lasers; optical mixing in non-linear crystals [2], or photomixing [3], among others. There are also sources based on quantum cascade lasers [4], formed by regularly repeated energy levels and capable of generating intrinsic THz radiation. Other recent works have developed THz generation with the use of resonant cavities [5], or even Fabry-Perot microresonators [6]. Thanks to the new advances, this spectral range has opened a new field of study of great interest for researchers, due to the great number of applications that have come to reality in numerous sectors, such as communications, space, security, or medicine, among others [7], [8]. This interest has

arisen mainly by certain peculiar properties available in this range, among which can be mentioned:

- Unique absorption features of organic molecules that allow distinguishing them from any other material, making possible the identification of dangerous materials from non-hazardous ones, even having similarities in terms of appearance.

- Ability to penetrate through materials with high resolution. This feature is used at airports, in modern see-through-cloth radars.

- The larger bandwidth allowed by the THz carriers and the small antenna sizes make this frequency range very interesting for communications.

- THz is a non-ionizing radiation, which is an advantage in medical diagnosis, because of the non-harmful exposure to these waves.

1.2. Thin-film sensing at THz

In the last years, sensing has become one of the most interesting THz applications, because many substances and materials exhibit molecular vibrations that are unique in this range, leading to the proposal of new high-performance detection devices. To date, several sensing platforms have been proposed, based on frequency selective surfaces [9], spoof plasmons [10], or metamaterials [11], among others. One of the biggest challenges of THz sensing is the detection of very thin samples, called thin-films, which are not detectable by classical systems due to measurement uncertainty. As

explained in a recent review [12], there are many cases where THz thin-film sensing research is critical or even the only option, among which can be highlighted:

- When the amount of the sample to characterize is very small.
- When the easiest way to process the sample is in the thin-film form, such as in the case of chemical or biological monolayers.
- When a thin-film sample has different properties from its bulk counterpart.
- When the quality parameter such as the sensitivity is better using a thin-film.

The objective of any sensing device is the identification of the presence of some amount of analyte (a material, sample, or tissue that we want to characterize) in the sensor, which should introduce some measurable change of the properties on the empty structure. This change may be the frequency at which the resonance happens, or a change in the amplitude, or any other measurable parameter. Resonant devices, such as the ones studied in this work, typically experiment a shift in its resonant frequency (Δf) when an analyte is deposited on them.

The key parameters that allow us to quantity the performance of any sensor are its sensitivity (S), and Figure of Merit (FOM). The sensitivity is a parameter defined by the researcher, and hence there is not a universal definition. In any case, to be both useful and meaningful it but must be defined in such a way that allows deciding whether a sample can be detected unambiguously. In most thin-film applications the sensitivity is usually defined as the ratio between the variation of the resonance wavelength and the variation of the analyte thickness: $S = \Delta\lambda/h_a$, in which case it is unitless. It is important

to achieve a high sensibility to create a high quality sensor, but it is also important not just having high values of sensitivity, but also narrow peaks that allow discriminating the different resonances (see Figure 1.2). The FOM is a more accurate parameter to evaluate the overall quality of a sensor, as it is defined as the ratio between the sensitivity and the full width at a half minimum (FWHM), related with the width of a pulse, in wavelength dimensions: FOM = S/FWHM. A good sensor will present a high sensitivity, and a narrow spectral line, leading to a high FOM.

Different sensing platforms have been proposed along the last years, including waveguides, filters, resonators, and plasmonic structures. Metamaterials, or metasurfaces (the planar version of metamaterials) are emerging as a revolutionary alternative to the previously mentioned devices, due to the their simplicity and exciting properties they offer in comparison with classical solutions[12].

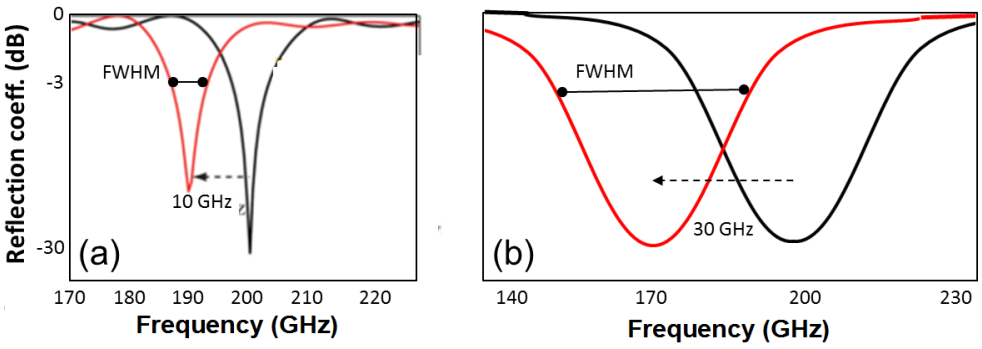

Figure 1.1. Reflection coefficient for two designs with different quality factor, (a) lower sensitivity but higher FOM, (b) higher sensitivity but lower FOM.

1.3. Metamaterials and Metasurfaces for sensing purposes

The first metamaterial definition was suggested by Roger M. Walser in 1999 as follows:

> *"Metamaterials are macroscopic composites having man-made, three-dimensional, periodic cellular architecture designed to produce an optimized combination, not available in nature, of two or more responses to specific excitation."*

The term Metamaterial (MM) comes from the Greek world "meta" (meaning beyond), and refers to materials that have properties not available in nature. These artificially created materials have their origin in 1968, when Veselago proposed for the first time a medium with negative values of both permittivity and permeability [13]. He found that in this media the phase and group velocity are in opposite direction (antiparallel) and the electric field (**E**), magnetic field (**H**), and wavevector (**k**) form a left-hand triplet, which means that they follow the left-hand rule instead of the right-hand rule characteristic of classical materials. This leads to interesting properties like inverse Snell´s law (see Figure 1.3(a)), or inverse Doppler effect, among others.

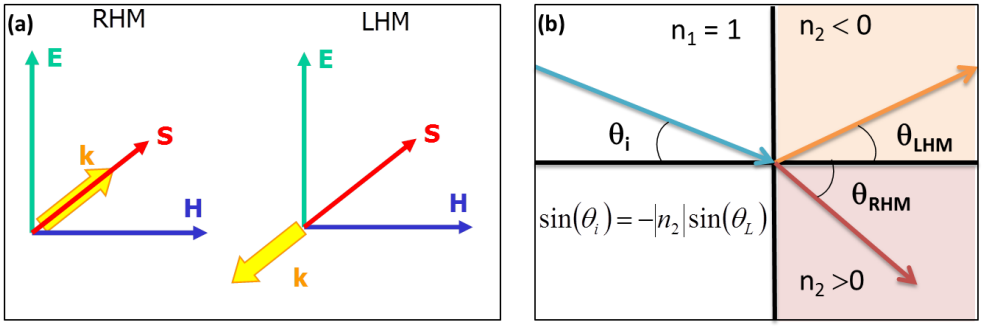

Figure 1.3. (a) Left-handed triplet and right-handed triplet representation, where **E** and **H** are the electric and magnetic field respectively, and **k** the wavevector. (b) Schematic of Snell's law in a media with positive refractive index and in a media with negative refractive index.

Later, in 1999, Pendry proposed a subwavelength structure using non-magnetic components, the Split Ring Resonator (SRR), with a strong magnetic response [14], able to produce a negative permeability within a narrow frequency band around the first resonance. The first experimental demonstration of metamaterials was carried out by Smith in the year 2000, with the synthesis of a medium with both negative permittivity and permeability [15]. This prototype was based on the combination of a matrix of SRRs, with negative permeability; and an array of thin straight wires, with negative permittivity. The combination of both elements presented a frequency response with a peak of transmission. It was also in the year 2000 when Pendry revolutionized the MMs research by proposing a lens with (ideally) infinite resolution, called Pendry's lens, and composed of a slab of negative refractive index material (with $\mu = \varepsilon = -1$, where μ is the magnetic permeability, and ε the dielectric permittivity). Another great landmark in the history of MMs was the achievement of the invisibility cloak, by the development of MMs able to deflect electromagnetic waves so that they do not interact with the concealed object, making it invisible to the observer [16]. Even though the initial studies had imperfections with bulky devices that targeted mostly the lower-frequency part of the spectrum, principally microwaves [17], this has become a very interesting

field of study, and recently there have been important advances, such as studies in the visible spectrum using metasurfaces [18], [19]; or experimental demonstrations based in ultrathin carpet cloaks for millimeter waves [20].

Although along the years this definition has evolved enormously, MMs are still based on the idea of combining elementary particles with a desired electromagnetic response to achieve properties beyond natural materials. In electromagnetism, materials are characterized by their dielectric permittivity, ε, and magnetic permeability, μ. Depending on the sign of these parameters, we can distinguish among four different classes of metamaterials, as shown in Figure 1.4:

- **Double-positive metamaterials (DPS) or right-handed media**: both ε and μ are positive. This leads to a positive refractive index, $n > 0$, and the vectors **E**, **H**, and **k** form a right-handed triplet. Most of the dielectrics available in nature can be categorized in this group.

- **Double negative metamaterials (DNG) or left-handed media**: both ε and μ are negative. This leads to a negative refractive index, $n < 0$, and the vectors **E**, **H**, and **k** form a left-handed triplet. These materials have interesting effects, such as inverse Snell´s law, or reverse Doppler effect, among others.

- **Negative permittivity media (ENG)**: where ε is negative and there is no propagation.

- **Negative permeability media (MNG)**: where μ is negative and there is no propagation.

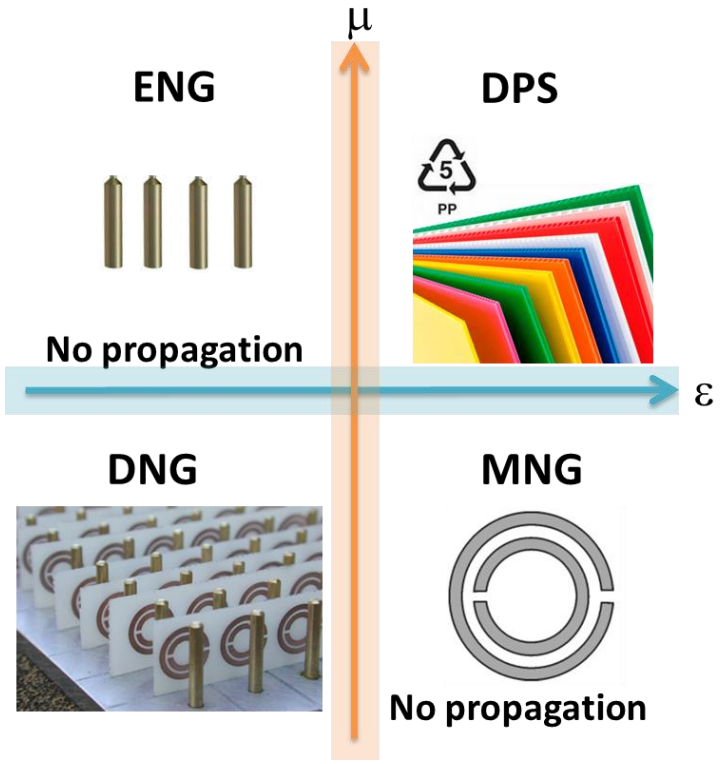

Figure 1.4. Classification of materials in the permittivity-permeability plane (real part).

Metamaterials and more specifically metasurfaces (the planar version of metamaterials) are becoming a revolution in sensing applications along the whole electromagnetic spectrum and especially at THz [12], [21], [22]. Metasurfaces can be defined as planar screens of periodic elements, generally metallic, designed to be transparent (or not) in some frequency bands while reflecting, or absorbing, to others. They are generally designed by assembling arrays of resonators whose size and spacing between them are much smaller than the wavelength; and with geometric parameters that can be modified to create a desired frequency response. This means that they can easily be made resonant at THz frequencies by simply scaling them. By choosing the materials of the substrate and the pattern properly, we can control the phase of the

reflected, transmitted, or absorbed light at the interface between a host material (like air) and the metasurface.

Each resonator used for the design of a metasurface usually exhibits a Lorentzian resonance response when exciting it with an incident wave, what is equivalent to the response obtained from a lumped RLC circuit, with the capacitance, *C*, and the inductance, *L*, determined by the properties of the materials [12]. At resonance, each resonator produces a high concentration of the electric field, producing a sharp change in the spectral response, and highly sensitive to changes in the surrounding media. This allows for a high sensitive detection even with minute amounts of analyte, which means an important advantage to thin-film sensing analysis (see Figure 1.5).

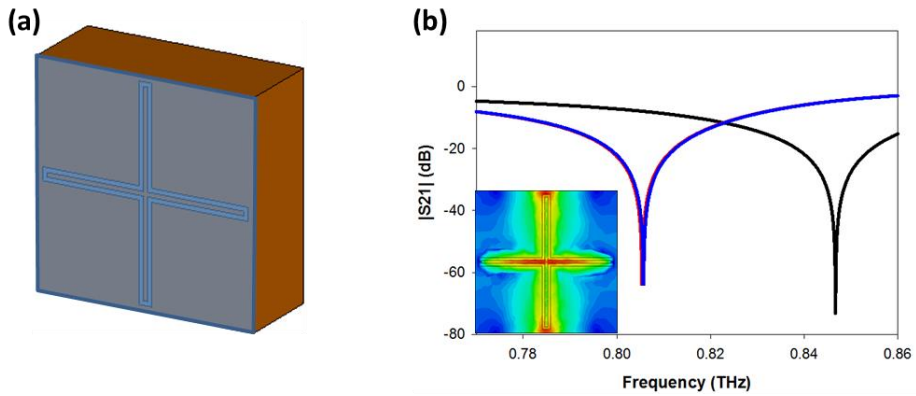

Figure 1.5. (a) Schematic of a cross-dipole metasurface with an analyte deposited on it. (b) Transmission coefficient for the unit cell presented in (a) with (blue line) and without (black line) analyte. Inset: high concentration of the electric field in the cross-dipole presented in (a).

Thin-film sensors based on metasurfaces exploit the strong field concentration existing in the gaps of the metallic patterns when the metasurface is at resonance with the objective of being capable to detect in a precise way the amount of sample, concentration, or thickness deposited. There are works in the literature that have studied the effect of the metal [23] and substrate [24] thickness on sensing purposes. The first

time that a metasurface was used was proposed by Driscoll to sense a silicon layer many times thinner that the skin depth of THz radiation [11]. Since then, similar designs have been studied [12], [22], [25]–[27]. The fabrication techniques such as lithography permit the fabrication of limited thickness metasurfaces, allowing us to obtain designs of a hundred of μm thickness [22], [28], [29]. These devices are capable of detecting a few hundreds of nm of analyte thicknesses, which usually saturates when depositing dozens of microns [22], [30]. Some of the pioneering works with historical importance are shortly described below:

- In 2010, Tao and co-workers designed a SRR based planar THz metamaterial working at 0.255 THz on an ultrathin silicon nitride substrate for biosensing applications, and observed a frequency shift of 10 GHz when depositing a 1.5 μm thick analyte [25].

- In 2012, Sabah [26] achieved a 70 GHz shift with an analyte of 10 μm using circular and squared SRRs in with structures of quartz glass as substrate and Al patterns, working at the frequency of 0.86 THz.

- In 2015, Cong et al. designed a cross-shaped perfect metamaterial absorber with a three-layer structure (silicon substrate, polyimide spacer, and aluminum pattern), with a resonance at the frequency of ~0.7 THz to use it as a refractometer with a 11 μm thick analyte [30], observing a maximum frequency shift of 77 GHz, as is shown in Figure 1.6 (a).

- The antennas group of this university also has experience in sensing at THz using metasurfaces. A cross-dipole structure working at the THz band (0.8 THz) was presented in 2016 [22] and its behavior as thin-film sensing and

refractometer (see Figure 1.6 (b)) was studied. This work is also a continuation of a final degree project [31], where various metasurfaces where designed and simulated.

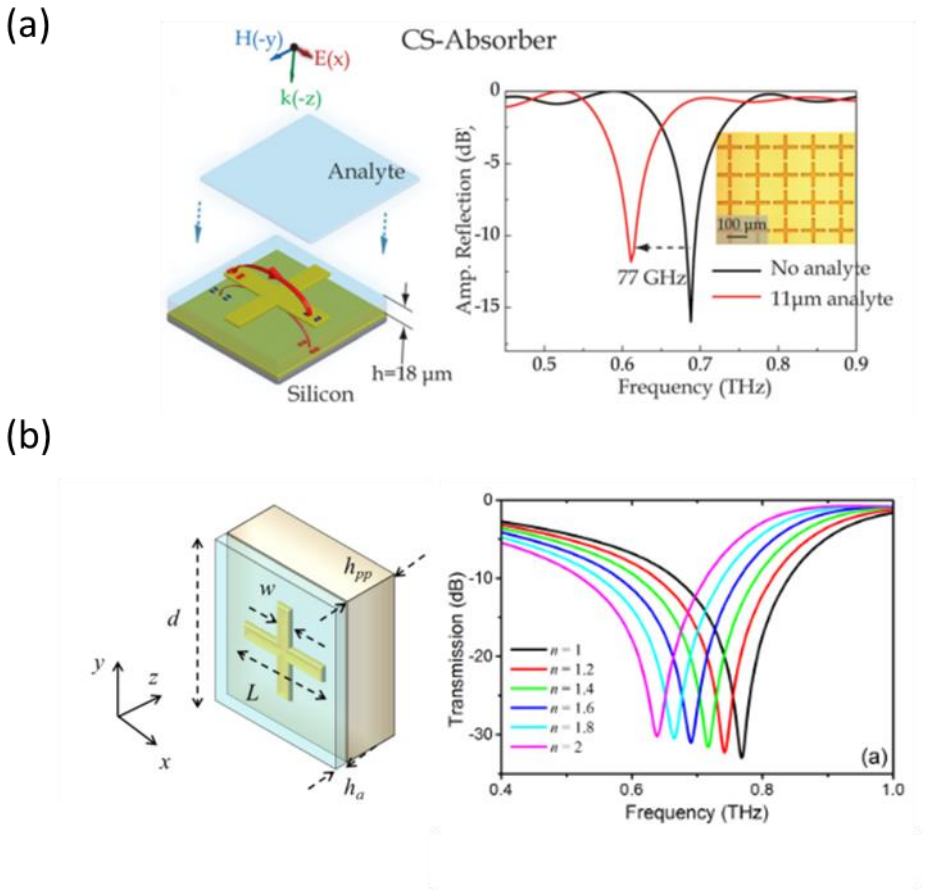

Figure 1.6. (a) Schematic of a cross-shaped perfect metamaterial absorber and its use as a 11 μm thick analyte sensing. (b) Cross-shaped structure working at the THz band and its use as refractometer.

1.4. Extraordinary Optical Transmission (EOT)

The extraordinary optical transmission (EOT) phenomenon was discovered for the first time in 1998, when T. W. Ebbesen and co-workers were analyzing two-dimensional arrays of circular apertures in metallic films. In this study, they found sharp peaks in transmission at wavelengths as large as ten times the diameter of the holes

[32]. They also noticed that these peaks of transmission took place in the cutoff regions of the holes, and named the phenomenon as *extraordinary optical transmission*. In 2000, Avrustsky et *al*. found that EOT appeared in a structure with only periodic corrugations [33]. The initial interpretation related the high transmittance peaks with the coupling of the incident light to surface plasmons, but it was soon noticed that similar peaks could be obtained assuming a perfect electric conductor model for the metal which, obviously, does not support plasmons [34]–[36]. This opened the way towards the replica of the phenomenon at frequencies in which metals do not follow a Drude model (typical of the plasmonic approach), such as millimeter-waves [37] where metals are usually described as good conductors with a high conductivity characteristic. Nowadays, EOT has been found all along the electromagnetic spectrum demonstrating that the phenomenon is general and not restricted to the infrared range [35], [36] and giving rise to disruptive technological applications such as structural color pixels [38], [39], metamaterial devices [40]–[42], etc. It is now well established [43], [44] that EOT occurs in array of subwavelength holes perforated in metallic films (see Figure 1.7 (a)) where the periodicity is much larger than the diameter of the holes. The EOT phenomenon refers to the appearance of peaks of transmission at certain frequencies below cutoff when the polarization is parallel to the large periodicity which corresponds to the regular EOT resonance. The EOT resonance happens when the distance between the holes in the structure is comparable to the wavelength and is much larger than the hole size. Additionally, if a rectangular cell is used and the structure is loaded with a dielectric substrate these structures can also support transmission below cutoff for the polarization parallel to the short hole periodicity, a phenomenon called anomalous EOT [44]–[46]. This is shown in Figure 1.7 (b) where a peak of transmittance appears in the cut-off region, before the minimum corresponding to a single anomaly, called Wood's

anomaly. This phenomenon was discovered by Wood in 1902, when studying a continuous light source given by an optical metallic diffraction grating. He noted that a null of transmission was observed when the magnetic field was parallel to the gratin grooves [47].

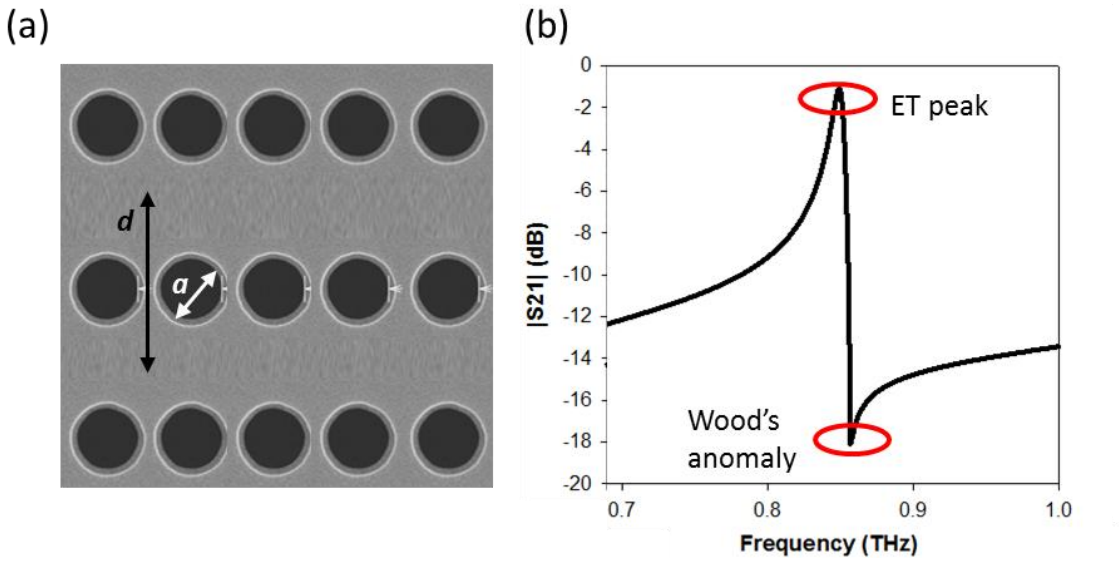

Figure 1.7. (a) Schematic of a hole array structure. Dimensions: polypropylene substrate height, h = 75 μm; unit cell vertical period, d = 350 μm; hole diameter, a = 105 μm. (b) Transmission coefficient of the hole array described in (a). Anomalous EOT.

As discussed in [45], [48] the appearance of the anomalous EOT depends on the dielectric slab characteristics (h_{PP} and ε_{PP}) as well as the large HA periodicity, d_y. More specifically, the anomalous EOT resonance cutoff can be calculated with the auxiliary factor $F = h_{PP}\sqrt{(\varepsilon_{PP}-1)}/d_y$. so that if $F \geq 0.25$, the anomalous peak will appear (see Figure 1.7(b)).

The high field intensity that arises near the subwavelength apertures at the EOT resonance is particularly well-suited for sensing applications, since the characteristics of substances placed near the hole array can shift strongly the resonance frequency. This sensing ability was demonstrated by Brolo *et al.* in the visible spectrum using arrays of

nanoholes in a gold film loaded with a monolayer of a solution of 11-mercaptoundecanoic acid [49]. This result spurred the investigation on sensing devices based on EOT hole arrays [50], [51], leading to a rapid evolution of the topic. It has matured all over the years and nowadays one can find in the literature a high variety of examples, some of them with advanced functionalities such as biosensors able to provide a quantified measurement of biomarkers related with cardiac diseases in human serum [52]; sensors combining nanofluidics and nanoplasmonics with a high throughput even with small amounts of analyte [53]; and even sensing platforms similar to the previous one, coated with group-specific antibodies to achieve a direct detection and monitoring of viruses [54]. There are excellent reviews in the recent literature accounting for the latest progress in this exciting and expanding topic, mainly centered in the infrared regime, where EOT is combined with surface plasmons for enhanced sensing platforms [55]–[58]. In this work, we have studied the anomalous EOT in hole arrays. Due to its sharp resonance in comparison with the regular EOT, we believe that can be suitable for thin-film sensing purposes.

1.5. Outline

In this work different types of metasurfaces are presented and its behavior as thin-film sensors is evaluated and compared with other devices found in the literature. This document has been organized as follows:

- In Chapter 2, the material and methods used to carry out this work are explained.

- Chapter 3 contains all the results of this work. This chapter is divided in sections depending on the structure under study.
    - In Section 3.1 a labyrinth metasurface sensor operating at the THz band is presented, and its behavior as SnO_2 thin-film sensing is numerically and experimentally evaluated and compared with other works that can be found in the literature.
    - In Section 3.2 two different hole array structures are designed, both operating at ~0.85 THz. A comparison between the regular and the anomalous EOT resonances is also presented and its performance as thin-film sensing devices is studied.

- Finally, the conclusions of this study and future work in the field, along with the bibliography used in this work and the author's merits are presented in the last chapters of this document.

Chapter 2

Methodology

2.1. Numerical simulator: CST Microwave Studio®

CST Microwave Studio® (CST MWS) is an electromagnetic full wave simulation software founded in 1992 by Thomas Weiland. It was an evolution of the MAFIA packet software: "solving Maxwell's equations using the Finite Integration Algorithm", introduced in 1977, based on the Finite Integration (FIT) technique [59].

CST MWS contains several solvers to best suit a given problem class (transient solver, frequency domain solver, eigenmode solver, resonant solver, integral equation solver, asymptotic solver, and TLM solver). To solve the electromagnetic problem, the simulation domain is first divided in small cells, wherein Maxwell's equations are solved. The program offers different meshing options, being the main ones hexahedral and tetrahedral mesh. With the hexahedral mesh, the whole simulation domain is divided into small cubes (either uniform or of varying size) whereas with the tetrahedral mesh, only the objects are divided in small tetrahedrons and the rest of the simulation domain is left unmeshed. Due to the intrinsic features of each mesh type there are some fundamental differences. The most relevant difference for this project is that hexahedral meshes do not conform to material jumps whereas tetrahedral ones conform to solid-boundaries and consequently to material jumps. The mesh influences the accuracy and speed of the simulations. Small mesh cells usually lead to more accurate solutions but at

the expense of increasing the computation time and vice versa. Regarding hexahedral or tetrahedral performance, generally hexahedral meshes take shorter simulation time, whereas tetrahedral meshes are more accurate with the presence of small or curved dielectric solids. For these reasons, it is difficult to give a general statement of which mesh is better for a given problem class. Therefore, the software offers different mesh types depending on the solver type used.

Regarding the type of solvers available in CST, the frequency domain solver is a general purpose simulator. It delivers electromagnetic near- and far-fields as well as S parameters, among other electromagnetic parameters. Although the transient solver also delivers broadband frequency results like S parameters, the frequency domain solver is preferable for the calculation of electrically small structures or with high Q-value. It can work with hexahedral or tetrahedral meshing, although the latter is usually preferable. The frequency domain solver is also ideally suited (in fact, the only choice in CST) for periodic structures.

In this work, all the problems under study are based on planar periodic structures, so all simulations in this work were performed using the frequency domain solver. To model the structure as an infinite array, the regime of Floquet ports and unit cell boundary conditions applied to the designed unit cell was employed. A fine tetrahedral mesh was applied to resolve properly the details of the metallic patterns used in the structures under study as well as the fine analyte layer used to measure the sensing capability of the sensors proposed. The metallic patterns as well as the ground planes (when used) were modelled as aluminum (Al) with electric conductivity σ_{Al} = 1.5×10^7 S/m. The more than twofold conductivity reduction versus to the bulky aluminum (3.6×107 S/m) is explained by the inherent roughness of metallic parts. The

dielectric substrate was modelled as polypropylene (PP) with different thicknesses depending on the case of study with a dielectric permittivity, ε_{PP} = 2.25 and loss tangent, $tan\delta_{PP}$ = 0.001. The analyte used in the labyrinth structures was modelled as a thin layer of tin dioxide (SnO2), with permittivity at the operation wavelength, $\varepsilon_{Sn02} \approx 4$, and variable thickness from 24 nm to 350 nm. Additionally, the analyte used in the hole array structures was modelled as a dielectric of variable thickness from 3 μm to 13 μm and a complex permittivity shown in Figure 2.1.

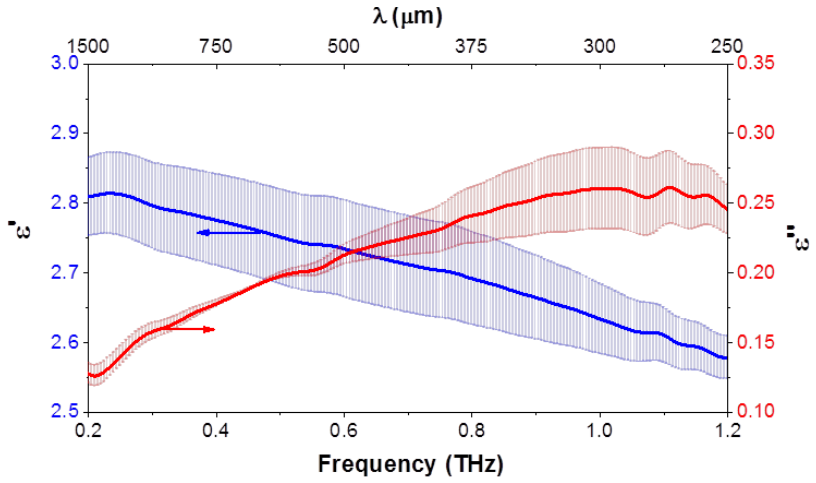

Figure 2.1. Measured frequency response of the complex analyte permittivity, with error bars: real (blue, left axis) and imaginary (red, right axis) components.

2.2. Experimental measurements: ABmm VNA analyzer

For experimental measurements of the fabricated metasurfaces the Vector Network Analyzer (VNA) MVNA-8-350-4 available in the Antennas Group – TERALAB of UPNA has been used. This analyzer covers the frequency range from 8 GHz to 1 THz, and it measures the complex, (or vector) impedance in the millimeter

and sub-millimeter frequency domain. The detection system includes a tunable microwave source and a detector, frequency stabilization unit, data acquisition and data processing system. It provides both the amplitude and phase of the transmitted and reflected signal. The MVNA used in this work is shown in Figure 2.2 (a).

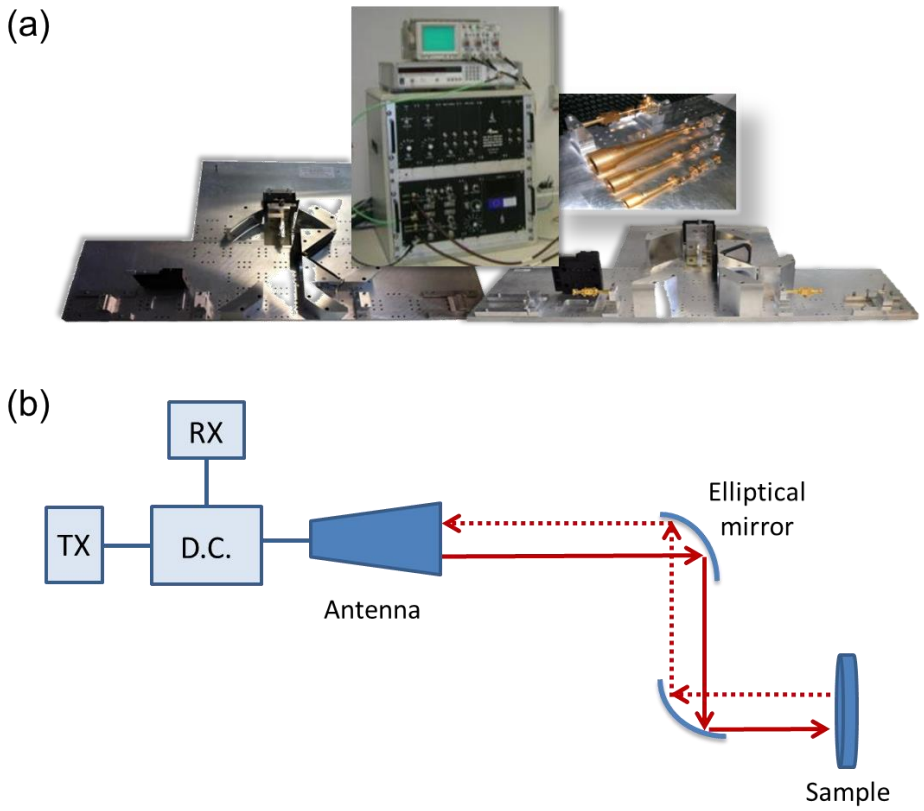

Figure 2.2. (a) UPNA's MVNA-8-350-4. (b) Scheme of MVNA operation in reflection configuration.

The measurements of the labyrinth metasurfaces were performed in the D-band of the millimeter-wave spectrum that extends from 110 to 200 GHz. The principle of operation can be described as follows (see Figure 2.2(b)): a vertically polarized pure Gaussian beam is transmitted by a corrugated horn antenna, with a beam radius of 12.9 mm. A pair of elliptical mirrors is placed in the beam path to collimate the beam at the location of the sample. Then, the beam is reflected back to the mentioned elliptical

mirrors. In this case, the reflection configuration was employed, so that the source antenna also works as the receiver for the reflected signal. This is possible by using a directional coupler that steers the signal to the receiver. Before measuring the sample, it was necessary to calibrate the system. The calibration in the reflection configuration was done by removing the sample from the sample holder and placing a mirror instead. The sample was carefully placed at the proper phase plane by adjusting the z position with a precise micrometer screw.

Measurements of the hole array structures

The transmission spectra of the hole array structures were measured with a custom-made THz time-domain spectrometer (TDS) developed in the Laboratory of Informational Optics at the Institute of Automation and Electrometry SB RAS (Novosibirsk, Russia). The THz-TDS schematic is shown in Figure 2.4. The setup utilizes a compact femtosecond Er-doped fiber laser combined with a second harmonic generation module (Toptica Photonics, Germany), which delivers the average power of 80 mW at 775 nm and 130 fs pulse duration. Laser radiation is split into two beams: 90% to pump an interdigitated high power multi-slit dipole antenna iPCA-21-05-1000-800-h (Batop GmbH, Germany), and 10% to probe the THz radiation with a conventional electro-optical sampling technique [60], [61]. A voltage generator modulates the THz radiation at 8 kHz by switching the antenna's voltage (±15 V). The emitted THz waves are collimated into the beam with a diameter of about 15 mm by an off-axis parabolic mirror and then focused by a similar mirror into the (110) cut 2-mm thick ZnTe crystal with an antireflection coating optimized for the wavelength of 775 nm. The reference frequency of the lock-in amplifier is locked to one of the voltage generator. Custom-developed software records the waveform of THz pulses by

controlling the optical delay line and receiving the signal from the lock-in amplifier. The developed THz-TDS covers the spectral range of 0.1–2.5 THz, while its dynamic range exceeds 75 dB at the frequency of 0.3 THz.

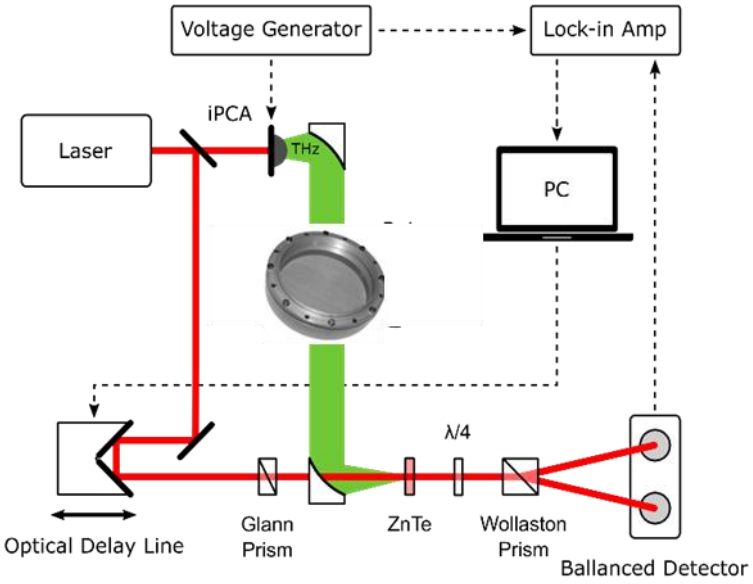

Figure 2.4. Schematic of the THz time-domain spectrometer. Red lines – laser radiation; green – THz radiation; black line with arrows – translation stage travel direction; dashed lines with arrows – electrical signals flow direction.

2.3. Manufacturing techniques

Fabrication of the labyrinth metasurfaces

The metasurface was lithographically patterned in a 0.4 um thick aluminum (Al) layer sputtered on the PP film 50 um thick via a vacuum thermal deposition method. Prior to sputtering, the PP film was treated with a glow discharge in argon atmosphere to improve adhesion of Al to PP. For patterning we employed a contact photolithography technique, which was specifically adapted to flexible solid film substrates, such as PP, whose industrial production does not allow obtaining a liquid phase suitable for posterior film deposition via spin coating [62]. After photolithography, a continuous aluminum layer 0.4 um thick was sputtered on an unpatterned side of the PP film to form the ground plane layer of the metasurface.

The metasurface dimensions were chosen from the conditions imposed by our fabrication and instrumental capabilities, as explained below:

- The widths of metallic lines and inter-line gaps in the metasurface pattern were required to fall within the range of 10±2 um.
- The free-space wavelength λ_0 of the fundamental absorption resonance for the metasurface was made as large as possible without exceeding 2.5 mm.

Analyte deposition and thickness characterization: labyrinth metasurfaces

The metasurfaces were pretreated with oxygen plasma and then coated with SnO_2 thin films by sputtering [63] using a DC-sputter coater (Quorum Emitech K675XD, from Quorum Technologies Ltd.) with a partial pressure of argon of 8×10^{-2} mbar and a current intensity of 90 mA. The SnO2 target used was purchased from Plasmaterials,

Inc. (99.9% purity). The deposition times were incrementally changed in order to fabricate thin films with different thicknesses. The thickness of the SnO2 thin films were measured experimentally by a profilometer (DeltaXT, from Brucker).

Fabrication of the hole array metasurfaces

For manufacturing the PP-film-backed hole array structures, a standard contact photolithography technique (CPhLT) described in [62] was utilized. CPhLT was specifically adapted to flexible solid PP substrates, whose industrial production does not allow obtaining a liquid phase suitable for posterior film deposition via spin coating.

The main stages of PP-based CPhLT are illustrated in Figure 2.3. Fabrication starts from tight mechanical fixation of the PP film on the bearing glass wafer (1) with the outer dimensions of 102×102 mm. The PP film is further treated with a glow discharge in argon atmosphere and then metalized by 0.4 μm thick aluminum via a thermal vacuum deposition method (2). The metallization procedure is followed by spin coating a positive photoresist film 0.6 μm thick, which is then air dried and thermally treated in a thermostat at 90°C (3). After putting the photoresistive layer into a hard contact with a structure's "positive" photomask represented by a quartz wafer with a patterned ferric-oxide-film (4), the photoresist is exposured to monochromatic UV-radiation (λ=365 nm) through the photomask (5) to create a latent image, which topological micro-pattern replicates the micro-pattern of the photomask. The latent image is further chemically developed in the solution of potassium hydroxide, which removes the irradiated (transparent) areas of the photoresist (6). Subsequent hardening of the developed photoresist by compressed air drying and thermal treatment at 120°C (7) forms the firm resistive mask, through which the Al-layer is further chemically etched by inorganic solvents (8). After removing the hardened resistive mask by its

dissolving in an organic solvent (9), the PP film with a fabricated metalized micro-pattern of the desired structure is separated from the glass wafer (10). At the final fabrication stage the hole array structure is tightly tightened onto a ring-shaped aluminum holder with the clear aperture diameter of 50 mm (11).

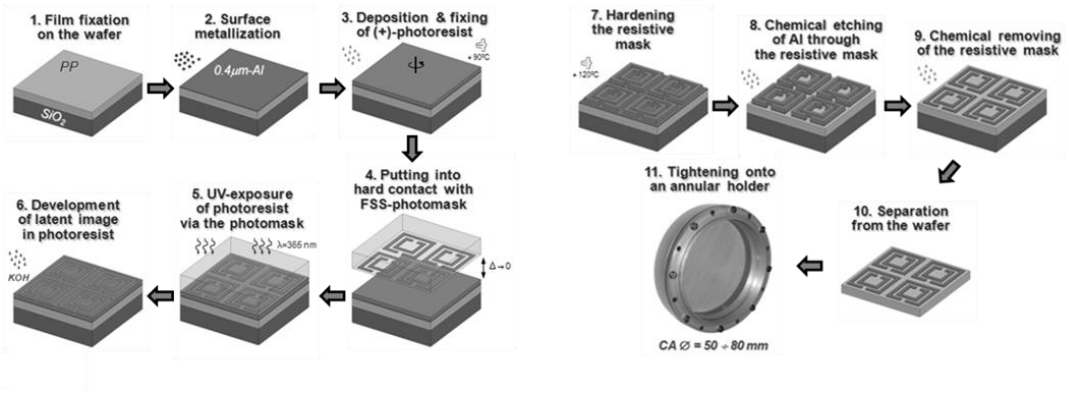

Figure 3.3. Fabrication stages for PP-film-backed THz-FSS by contact photolithography (an example of the SRR structure is shown).

Chapter 3

THz metasurfaces sensors

3.1. Labyrinth structures

In this section a labyrinth metasurface sensor operating at the low-frequency edge of the THz regime is presented. This intricate shape leads to a high electric field confinement in the surface of the structure, leading to ultrasensitive performance, able to detect samples of the order of tens of nanometers at a wavelength of the order of millimeters (i.e. 5 orders of magnitude larger). The sensing capabilities of the metasurface are evaluated numerically and experimentally by covering the metallic face with tin dioxide (SnO2) thin films with thicknesses ranging from h_a = 24 nm, to h_a = 345 nm. A redshift of the resonant frequency is observed as the analyte thickness increases, until reaching a thickness of 20 μm, where the response saturates. Our strategy is based on the convoluted geometry of a labyrinth-shaped micro-pattern that improves the field concentration all along the metasurface and not only at discrete spots, unlike the sensors based on canonical periodic structures. This shift from meta-atoms to more elaborated meta-geometries allows the detection of exceedingly thin dielectric samples deposited on top of the metasurface, with thickness and thickness increments in the nanometre scale at an operation wavelength in the millimetre scale. Hence, the developed sensor is able to discern films as thin as $\sim 10^{-5}\lambda_0$, with λ_0 the free-space operation wavelength.

Design and measurement of the empty structure

The unit cell of the labyrinth metasurface absorber with relevant dimensions as well as a microscopic image of the fabricated structure is shown in Figure 3.1(a) and (c) respectively. The metasurface consists of a triangular-lattice array of convoluted-shaped apertures manufactured as a continuous aluminum layer lithographically patterned on a polypropylene (PP) slab with uniform back metallization (i.e. ground plane (GP)). Each elementary aperture is designed as a center-connected strip element having 120° rotational symmetry. The choice of PP is explained by its small loss tangent value ($\tan\delta \approx 1\times10^{-3}$) in the THz domain that enables enhancing the Q-factor of the metasurface absorber [64] and therefore maximizing the FOM of the metasurface sensor (which is proportional to the Q-value [65]).

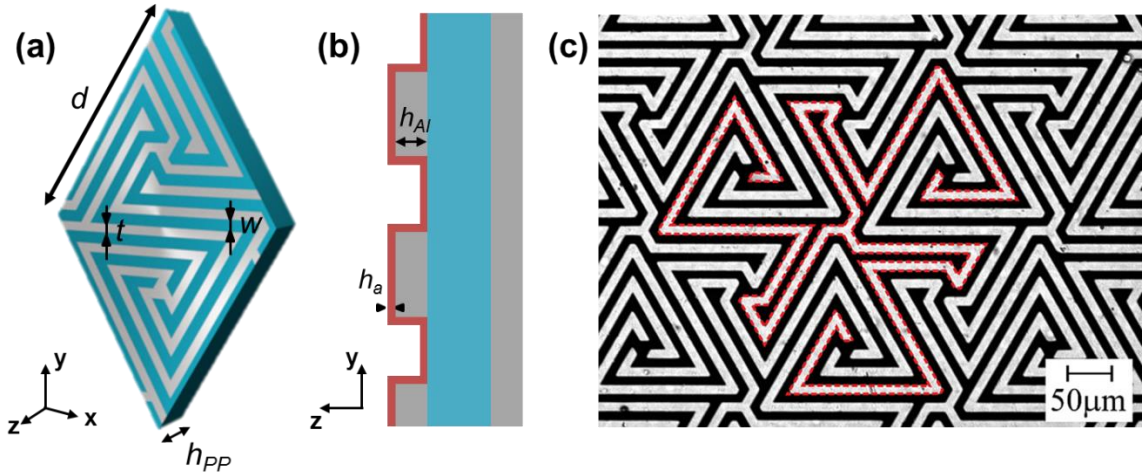

Figure 3.1 (a) Front view and (b) cross-section of the metasurface unit cell. In (a) the analyte has been omitted for clarity. Dimensions: d = 231 µm, h_{Al} = 0.4 µm, h_{PP} = 50 µm, t = 8.9 µm, w = 11.1 µm, h_a = 24 nm; 58 nm; 108 nm; 345 nm. Metallization is shown in grey. (c) Microscopic image of the labyrinth pattern on the PP substrate. The red dotted lines delimit the boundaries of the elementary convoluted-shape aperture used for creating a periodic metallic pattern of the metasurface**.**

Originally, the labyrinth metasurfaces were developed for using without the GP-layer and were intended for filtering applications in diagnostic systems of millimetre-wave radiation generated in schemes with free-electron masing [66], [67] and electron-beam-induced emission from hot magnetized plasmas [68], [69]. The metasurface pattern was designed to fix the transmission passband near 75 GHz and achieve at the same time strong suppression around 150 GHz combined with the requirement of maintaining a super-stable spectral characteristic under oblique illumination (Figure 3.2). As it is known, the angular stability of a resonance in any periodic array improves when the resonance frequency f_{res} occurs far below the onset of the first diffraction order f_{diff}, i.e. when $f_{res} << f_{diff}$. In this regard, triangular lattices outperform square-lattice solutions given that f_{diff} can be $\sqrt{2}/3$ times higher. This is why a metasurface with a triangular unit cell was selected. The actual metasurface dimensions indicated in Figure 3.1 were chosen from the conditions imposed by our fabrication capabilities (see supporting information) and the aforementioned requirements on the filtering performance of the GP-free metasurface.

The underlying design principle for such metasurfaces is based on the fact that the convoluted geometry of the metallic strips and the inter-strip gaps noticeably increases their total length within the metasurface unit cell compared to non-convoluted geometries. From an equivalent circuit perspective [70], [71], this factor considerably augments the effective lumped inductance L and capacitance C of the structure and, therefore, induces a much more noticeable redshift of its resonant frequency f_{res} according to the relation $2\pi f_{res} = 1/(LC)^{1/2}$. As a result, a 20-fold reduction of the central frequency of the fundamental passband ($f_{res} \cong 75$ GHz) relative to the onset of the first diffraction order located at $f_{diff} = 1500$ GHz (assuming normal incidence) is achieved, yielding excellent angular stability as shown in Figure 3.2 .

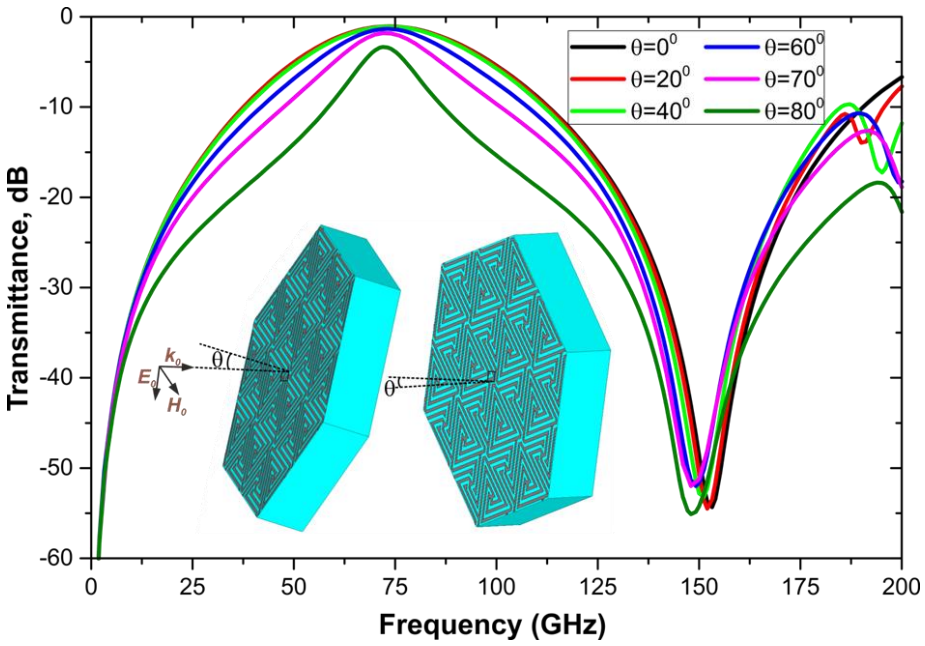

Figure 3.1. Simulated spectral transmittance of the GP-free 50um-PP-backed labyrinth metasurfaces in a bilayer multiplex (non-interference) configuration at different angles of incidence θ. To avoid inter-layer interference the indivual metasurfaces are inclined in mutually orthogonal planes with respect to the impinging wave. The resulted transmittance of such a bilayer structure is evaluated as a product of the single metasurface transmittances for TE- and TM-polarizations that is plotted here.

Prior to analyzing the sensing performance of the labyrinth metasurface in the absorber regime (i.e. after adding the GP-layer), we will analyse first the metasurface absorber without any analyte on top assuming normal incidence and both vertical and horizontal polarizations. As the GP blocks any transmission, we will only consider the reflection coefficient – both copolar and crosspolar components – in the following. We start the study with the lossless case, green curves in Figure 3.3. As shown there, the reflection coefficient magnitude is nearly 1 (solid green) all along the spectrum, except at $f \cong 137.6$ GHz where a small cross-polarization peak appears (dashed green). When losses are considered, a sharp resonance dip appears at $f_0 = 135.3$ GHz (solid blue

curve). The dip is caused by energy dissipation in the metasurface (which occurs mainly in the convoluted metallization) and not by cross-polarization of the reflected wave, as demonstrated by the low magnitude (less than −49 dB) of the crosspolar reflection coefficient magnitude (dashed blue curve). It is to be noticed that the absorption resonance is positioned near the stopband resonance of the GP-free metasurface, i.e. almost doubly exceeding the central frequency of 75 GHz of its fundamental passband (Figure 3.2). This is explained by the fact that the near-unity absorptivity for any metasurface absorber patterned on an electrically thin GP-backed dielectric layer can be attained only at frequencies where the impedance of the patterned layer is capacitive [64], [72]. Unlike the conventional meta-absorbers with electrically isolated metallic elements (e.g. patches) forming the top patterned layer whose low-frequency impedance is always capacitive, the labyrinth pattern considered here consists of electrically connected convoluted metallic stripes whose impedance at low frequencies is fundamentally inductive. The capacitive component in the stripes' impedance, however, becomes dominant over the inductive one above the passband (but below the stopband resonance) that allows fulfilling the absorber criterion.

Regarding the absorption performance of the structure, it should be noticed that a bare PP substrate has low dielectric losses and is very thin in terms of wavelength ($\lambda_0/44$). The full-wave simulations show that in the absorber configuration this feature is kept: the energy is dissipated mainly via ohmic currents induced in the metallic layer of the labyrinth pattern. This effect is illustrated in Figure 3.4 (a) where the fractional losses referred to the labyrinth pattern and the PP film are calculated as the functions of the normalized frequency, f/f_0. Furthermore, the response is independent of the wave polarization (the same happened for the lossless case). This was examined numerically by tracking the metasurface reflectance upon changing the E-field orientation angle for

the linearly polarized wave. The polarization angle varied from 0° to 90° with an increment of 10°. As seen from the results presented in Figure 3.4 (b), the metasurface spectrum remains unchanged at any polarization angle, which is an enormous advantage for sensing purposes. Therefore, we will hereafter assume only vertical polarization for all the upcoming calculations without loss of generality.

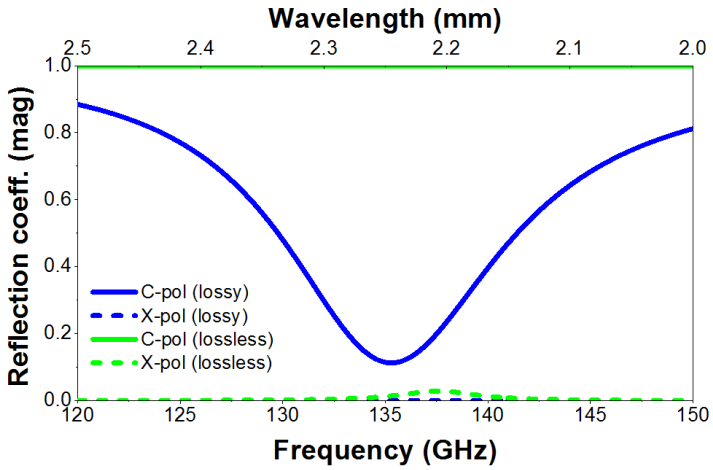

Figure 3.2. Reflection coefficient magnitude of the free-standing labyrinth metasurface absorber shown in Fig. 3.1. Lossless (green) and lossy (blue) scenarios are considered for both copolar (solid) and crosspolar (dashed) cases.

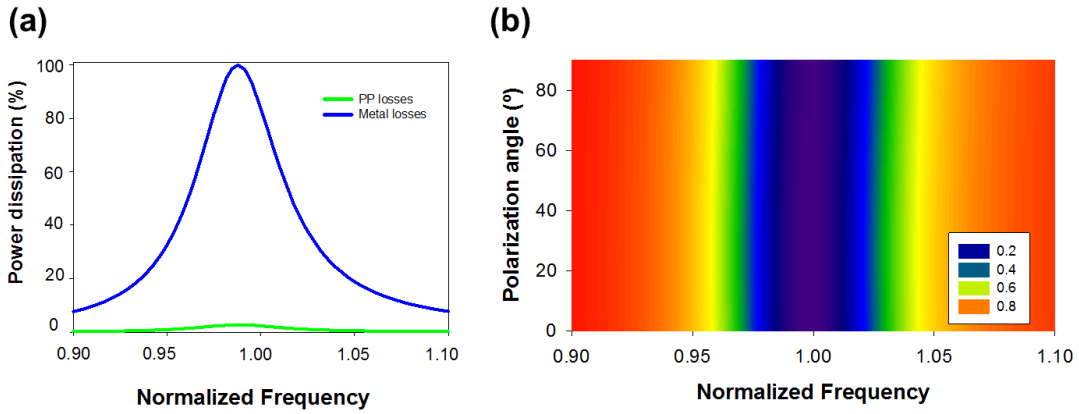

Figure 3.3. (a) Fractional power dissipation (in %) vs. the normalized frequency f/f_0 for the labyrinth metasurface absorber. Blue line: losses in metallization. Green line: losses in PP substrate. (b) Referred to the normalized frequency f/f_0, spectral reflectivity of the labyrinth metasurface absorber plotted as a function of the polarization angle for the impinging wave. Linear scale, normal excitation.

Design and measurement of SnO2 thin film sensor

Once the characteristics of the designed structure in the absence of analyte have been studied, the sensing capability of the metasurface is evaluated by coating the labyrinth face with different thicknesses, from 24 nm to 350 nm, of tin dioxide (SnO_2) thin films, whose permittivity is $\varepsilon_a \approx 4$ at the operation wavelength[73], [74]. The SnO_2 coatings were prepared by the sputter-deposition technique[63]. The experimental characterization was carried out with an ABmm™ Vector Network Analyser (VNA) MVNA-8-350-4 equipped with a quasioptical bench working in the reflection configuration. More information about the samples preparation and experimental methodology can be found in Chapter 2.

In Figure 3.5 is plotted the absorbance for several thicknesses of the SnO_2 film: h_a = 24 nm ($1.1\times10^{-5}\lambda_0$); 58 nm ($2.6\times10^{-5}\lambda_0$); 108 nm ($4.9\times10^{-5}\lambda_0$); 345 nm ($15.6\times10^{-5}\lambda_0$), numerical simulations in panel (a) and experimental measurements in panel (b).

From this figure it can be observed that a redshift of the resonance takes place when the analyte thickness increases. We also find that there is a good agreement between the numerical results (panel a) and the experimental measurements (panel b) in all the cases except when having an analyte thickness of h_a = 345 nm, where the displacement obtained in the experimental measurements is a bit larger than the one obtained on the numerical results. In any case, a maximum frequency shift of 4.89 GHz is obtained for the numerical results, and a maximum shift of 7.65 GHz is obtained for the experimental measurements, as shown in Table 1. From these results we can also obtain the wavelength shift as the analyte thickness is varied, displayed in Figure 3.6 (a).

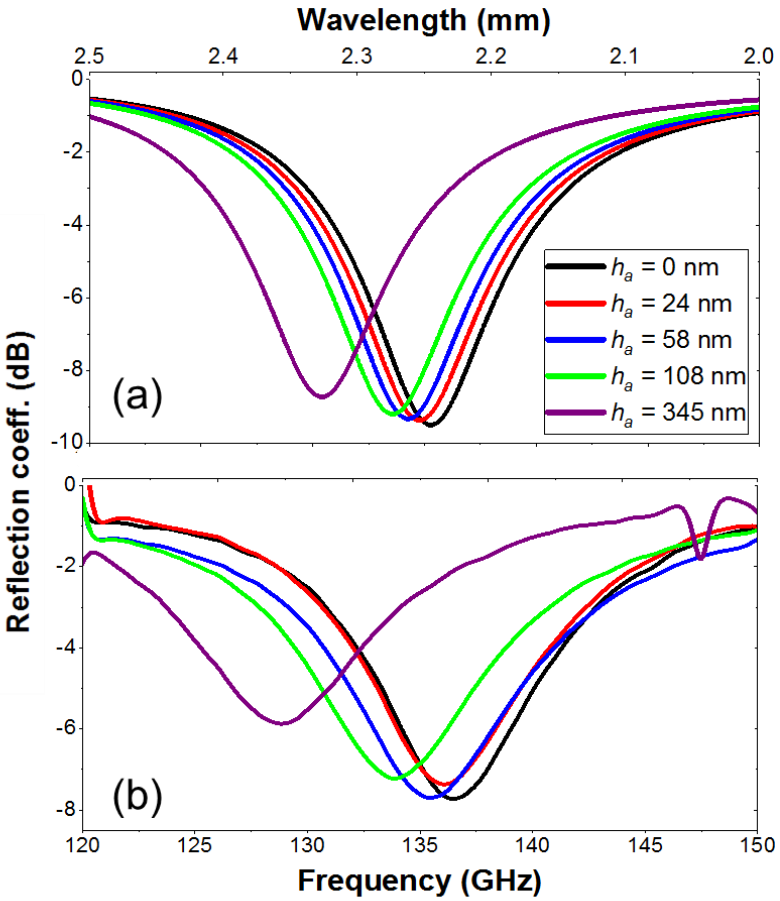

Figure 3.4. (a) Simulated and (b) experimentally measured spectra of the reflection coefficient for the labyrinth metasurface absorber under normal incidence and different analyte thicknesses.

It is noteworthy the extreme sensitivity of the labyrinth structure, able to discriminate differences in SnO_2 thickness of less than 25 nm even for a relatively low dielectric constant. In terms of the operation wavelength this means that the sensor is able to detect variations of only $\sim 1.1\times10^{-5}\lambda_0$, very much beyond the state-of-the-art sensing platforms which achieve, in the best case [25], a value around $1.7\times10^{-4}\lambda_0$. This is even more remarkable if one notices that the analyte does not fill completely the groove between metal strips, as sketched in Figure 3.1(b). We performed an additional simulation study increasing the analyte thickness and found that the response saturates when the thickness is nearly 20 µm ($0.009\lambda_0$) whereas for ultrathin analytes (h_a <

10 μm) the response is approximately linear. As a side comment, we can observe in the experimental curve of the sample with h_a = 345 nm a small dip arising at 147.5 GHz.

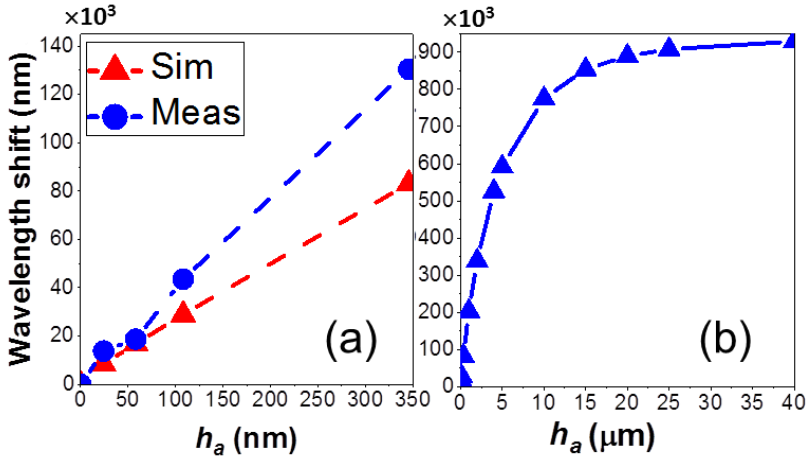

Figure 3.5 (a) Wavelength shift as a function of the analyte thickness for extremely thin analytes, simulation (blue) and measurements (red), calculated as $\Delta\lambda = \lambda_a - \lambda_0$, with λ_a the resonance wavelength at each h_a and λ_0 the resonance wavelength without the analyte. (b) Idem for more general analyte thicknesses, to show the saturation of the response (only simulation).

	h_a (nm)	f_{res} (GHz)	λ_{res} (mm)	Δf (GHz)	$\Delta\lambda$(μm)
Numerical results	0	135.3	2.217	-	-
	24	134.79	2.226	0.51	8.39
	58	134.28	2.234	1.02	16.84
	108	133.56	2.246	1.74	28.89
	345	130.41	2.300	4.89	83.14
Experimental results	0	136.5	2.198	-	-
	24	135.65	2.212	0.85	13.77
	58	135.35	2.216	1.15	18.67
	108	133.85	2.241	2.65	43.51
	345	128.85	2.328	7.65	130.49

Table 1. Behavior of the designed labyrinth metasurface for different analyte thicknesses. Numerical and experimental results.

We can quantify the performance of the sensor more formally by calculating its sensitivity (S) and FOM. As said in Chapter 1, the sensitivity relates the variation of the resonance wavelength with the variation of the analyte thickness: $S = \Delta\lambda/h_a$ where $\Delta\lambda = \lambda_a - \lambda_0$ with λ_a the resonance wavelength at each h_a and λ_0 the resonance wavelength without the analyte. Note that in refractometer applications the variation of the refractive index is also included but in our case we do not need to do this, as our aim is to detect only thickness variations. For the sake of completeness, a detailed comparative study of the sensor performance with other works in the literature using other sensitivity definitions is presented in the next sections. The FOM is defined as the ratio between the sensitivity and the full width at half minimum (FWHM) in wavelength dimensions: FOM= S/FWHM. A high FOM ensures a good resonance shift with analyte variation along with a narrow spectral line, avoiding overlap between different curves.

The values of the Sensitivity and FOM for the designed structure are presented in Table 2**.** They reach significantly high values both in simulation and measurement. In the experiment the maximum is obtained for h_a = 108 nm, where the sensitivity is ~ 870 and the FOM is ~ 4485 nm^{-1}. In the numerical results, the values are slightly lower, reaching a sensitivity of ~ 578 and a FOM of ~ 3027 nm^{-1}. These values are much higher than those found in the literature with similar fabrication techniques as the method used in this work, as it can be seen at the comparison made in the upcoming sections.

h_a (nm)	Sensitivity		FOM [nm^{-1}]	
	Sim	**Exp**	**Sim**	**Exp**
24	346.67	569.07	2028.66	3613.28
58	498.3	552.47	3027.77	4297.43
108	578.07	870.77	3558.51	4485.84
345	349.98	549.27	2351.44	4131.40
Average value	443.25	635.39	2741.6	4181.98

Table 2. Sensitivity and FOM for each analyte thickness for the sample described in the main text calculated as S = $\Delta\lambda/h_a$ and FOM = S/FWHM. Both simulation (Sim) and experimental (Exp) values are presented.

This excellent sensing performance of the labyrinth structure can be explained by its intricate geometry that provokes a strong electrical coupling between adjacent metallic strips. In very subwavelength structures, such as the one considered here, the electric field is strongly confined near the surface, so we can achieve high sensitivity to slight changes of the thickness of the thin-film layer deposited on top. To get a clearer view, we have obtained the electric field distribution of this structure at both sides of the labyrinth. As shown there, the field pattern is approximately symmetric at both sides of the metallization. Therefore, although there is indeed some field concentration inside the substrate, the field in the air interface is able to interact closely with the analyte. This is corroborated in Figure 3.6 (b) where it is shown that the saturation is reached for an analyte thickness of around 20 μm. Moreover, while in other sensing platforms the electric field starts to vanish at significantly larger distances, in the labyrinth structure the electric field starts to decline at only $5\times10^{-4}\lambda_0$ (corresponding to ~1 μm away from the metasurface outer face), where the magnitude of the electric power decreases to the

half (see Figure 3.7). Note that if we use denormalized values for the *x*-axis in panel (b), the value $0.01\lambda_0$, corresponds to 25 μm, which is the thickness where the response starts to saturate (see Figure 3.6 (b)). This highlights the importance of the electric field confinement for sensing purposes.

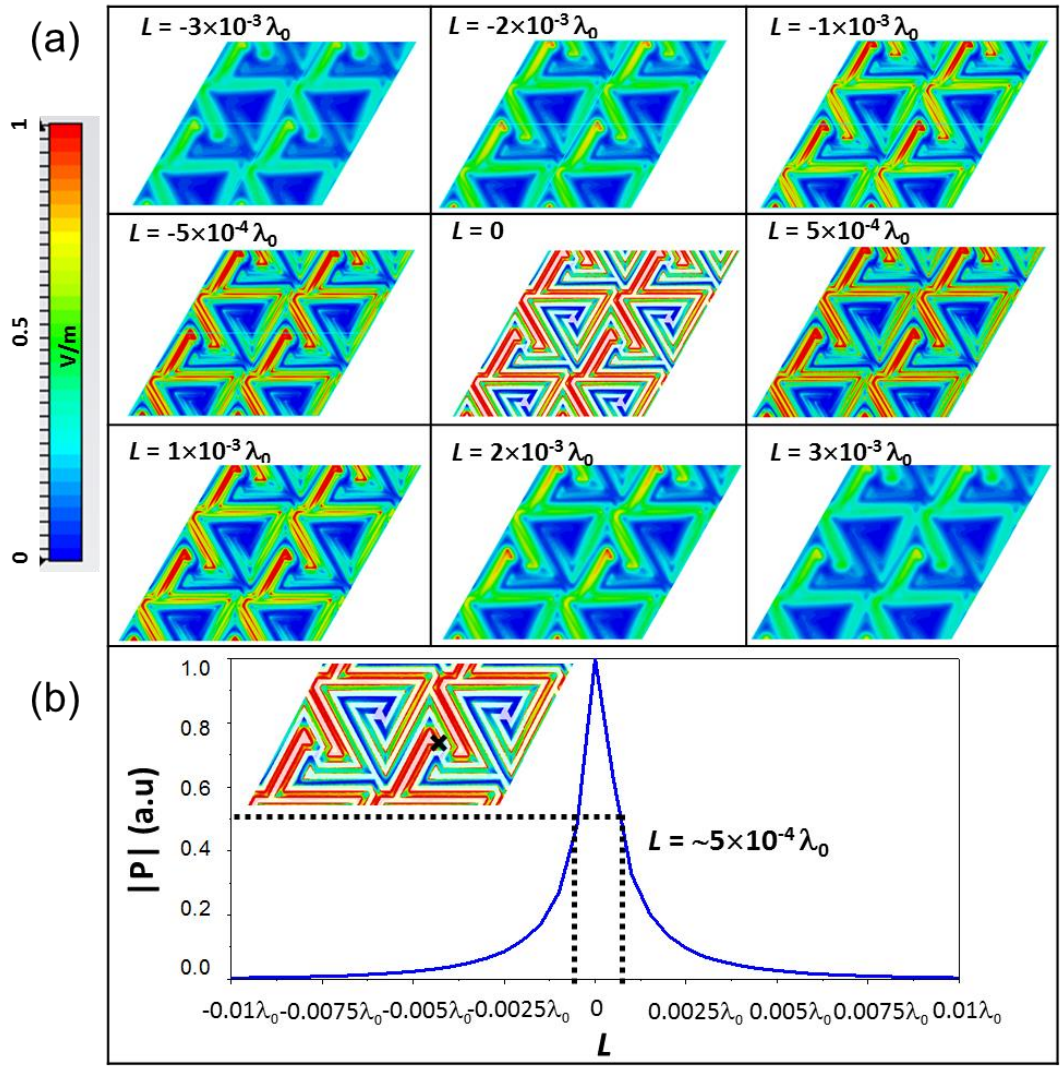

Figure 3.6. (a) Amplitude distribution of the electric field (absolute value) along the *z* axis at different distances (*L*, normalized to the operation wavelength) from the labyrinth metasurface absorber. (b) Normalized power vs. distance at the point indicated by a cross in the inset.

From all the above, it is clear that the labyrinth metasurface is quite promising for high sensitivity sensing applications. To ascertain its full technological potential, we

perform a repeatability study, using different metasurface samples, as well as a comparative analysis with other structures present in the literature to evaluate the performance in comparison with the state-of-the-art. These will be the topics treated in the following sections.

Study of an alternative prototype

In order to prove the repeatability of our measurements, we performed a complete study of another labyrinth sample (sample 2) by coating it with the SnO_2 analyte of thicknesses different than those used in the previous section (we will call this sample 1). The design of the unit cell is the same as the one shown in Figure 3.1, with the same PP substrate. It has to be noted that, due to fabrication tolerances, the labyrinth pattern of sample 2 has slightly different dimensions: t_2 = 8.2 µm, w_2 = 11.8 µm, instead of the values obtained in the sample 1, t = 8.9 µm, w = 11.1 µm. As the rest of parameters remain unchanged, the study of the empty metasurface can be omitted this time, as the behaviour is similar to the one of the sample 1. Figure 3.8 illustrates the sample's reflectivity for several thicknesses of the SnO_2 film ranging from h_a = 100 nm (4.55×10–5λ_0) to h_a = 250 nm (11.4×10–5λ_0) with a step of 50 nm, numerical simulations in panel (a) and experimental measurements in panel (b).

From the results shown in panels (a) and (b), one can trace a red shift for the reflectivity resonance when increasing the analyte thickness. Again, we can observe a good agreement between the numerical and experimental results in all the analyte thickness, except for a displacement in the resonance of the empty structure, which takes place at the frequency of 135.63 GHz in the numerical results, while in the experimental ones it takes place at 137.1 GHz. Leaving aside this small discordance, the

maximum displacement obtained in the numerical results is 2.67 GHz, while in the experimental results this shift is 2.98 GHz (see Table 3). The quantified values of this shift are displayed in Figure 3.9 (a). As reported in panel (b), the response saturates when the thickness approaches nearly 20 µm what repeats the result obtained with the sample I (see Figure 3.6 (b) in the main section). In total, the experimental data plotted in Figure 3.8 and Figure 3.5- demonstrate good repeatability of the measurements.

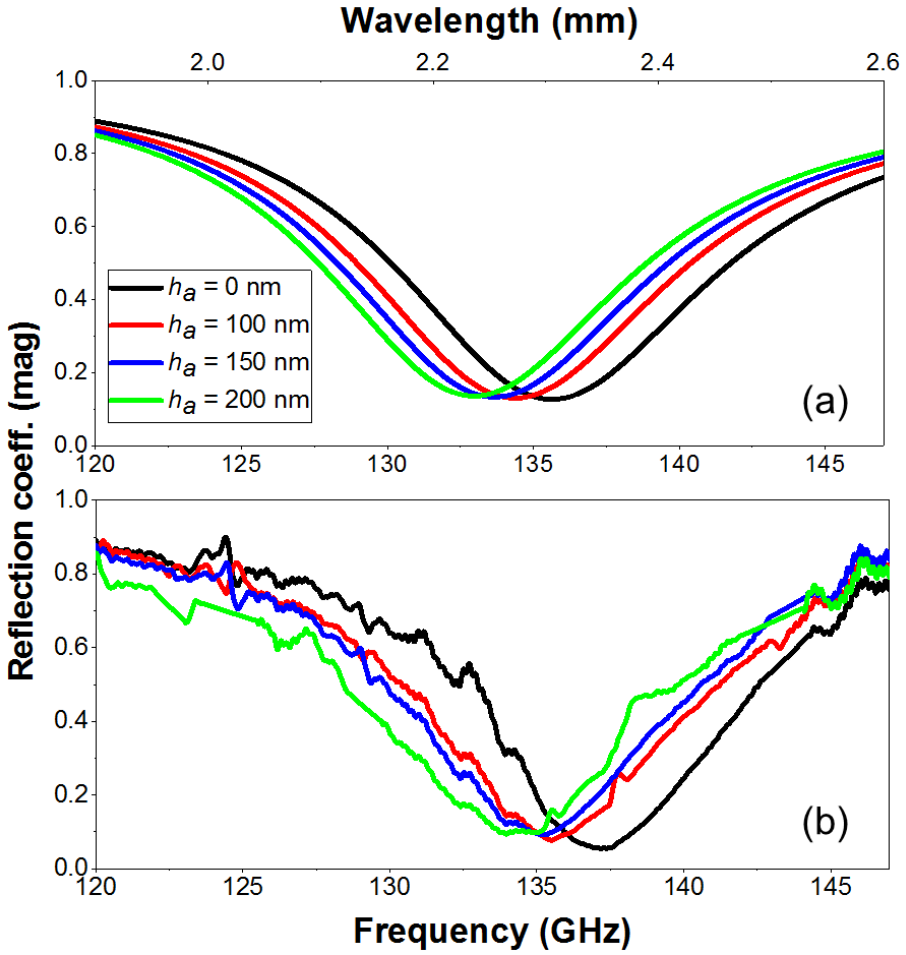

Figure 3.7. (a) Simulated and (b) experimentally measured spectra of the reflection coefficient for the labyrinth metasurface absorber (sample II) under normal incidence and different analyte thicknesses.

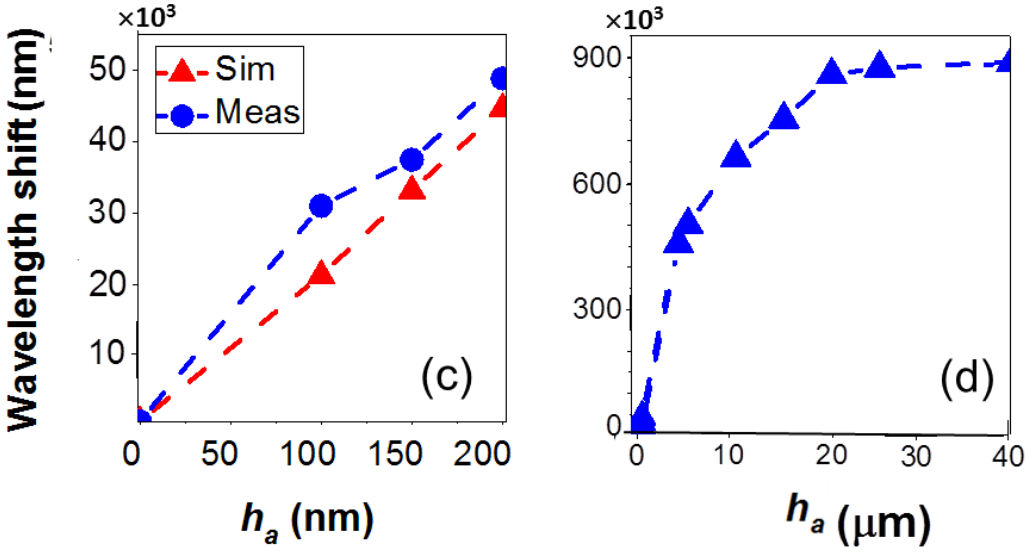

Figure 3.8. (a) Wavelength shift as a function of the analyte thickness for extremely thin analytes, simulation (blue) and measurements (red), calculated as $\Delta\lambda = \lambda_a - \lambda_0$, with λ_a the resonance wavelength at each h_a and λ_0 the resonance wavelength without the analyte. (b) Idem for more general analyte thicknesses, to show the saturation of the response (only simulation, sample II).

	h_a (nm)	f_{res} (GHz)	λ_{res} (mm)	Δf (GHz)	$\Delta\lambda$(μm)
Numerical results	0	135.63	2.212	0	0
	100	134.37	2.233	1.26	20.74
	150	133.65	2.245	1.98	32.77
	200	132.96	2.256	2.67	44.42
Experimental results	0	137.10	2.188	0	0
	100	135.21	2.219	1.89	30.59
	150	134.81	2.225	2.29	37.13
	200	134.12	2.237	2.98	48.68

Table 3. Behavior of the designed labyrinth metasurface for different analyte thicknesses. Numerical and experimental results.

We now calculate again the quality parameters, sensitivity and FOM: $S = \Delta\lambda/h_a$, FOM = S/FWHM. The values obtained are shown in Table 4. As before, the values reached in the experimental results are higher than those obtained in the numerical results. In the experiment the average sensitivity is ~265 and the average FOM is ~ 1926 nm^{-1}. In the numerical results, we have an average sensitivity of ~216 and an average FOM of ~1444 nm^{-1}. Although these values are a bit lower than those obtained in the main structure, they are still higher than those found in other works in the literature, demonstrating the repeatability of our designed metasurfaces.

ha (nm)	Sensitivity		FOM [nm-1]	
	Sim	Exp	Sim	Exp
100	207.41	305.89	1304.48	2257.52
150	218.46	27.57	1418.57	1793.96
200	222.08	243.42	1609.34	1725.13
Average value	215.99	265.63	1444.13	1925.54

Table 4. Sensitivity and FOM for each analyte thickness for the sample described in the main text calculated as $S = \Delta\lambda/h_a$ and FOM = S/FWHM. Both simulation (Sim) and experimental (Exp) values are presented.

Comparing sensitivity with alternative sensors

As said in the introduction chapter, sensing with metasurfaces has become a very interesting research field and there are many examples of metasurfaces working as sensors in the THz band. Although these examples work well as sensing platforms, they usually suffer from a relatively poor performance achieving small sensitivity values

compared with our design. Recently, new fabrication techniques have pushed forward the field by allowing the creation of nanogap structures [75], [76] able to achieve values of the sensitivity of the order of 4400 [75], at the expense of requiring a relatively complex manufacturing procedure. In this section we are doing a comparison with the two best structures found in the literature that use the same fabrication techniques as in our case, see Figure 3.10. Panel (a) shows the schematic and the electric field response of a square SRR metasurface designed by H. Tao *et al.* in 2010 [25], panel (b) shows two kinds of SRR metasurfaces designed by Sabah *et al.* in 2012 [26], and panel (c) shows a cross-shaped perfect metamaterial absorber proposed by Cong *et al.* in 2015 [30]. As it can be observed in Table 5, the maximum FOM amongst these works is 118 nm^{-1}, much lower than the values achieved by our structure (note that we have different results than the ones presented in the references due to our method to calculate the sensitivity and FOM).

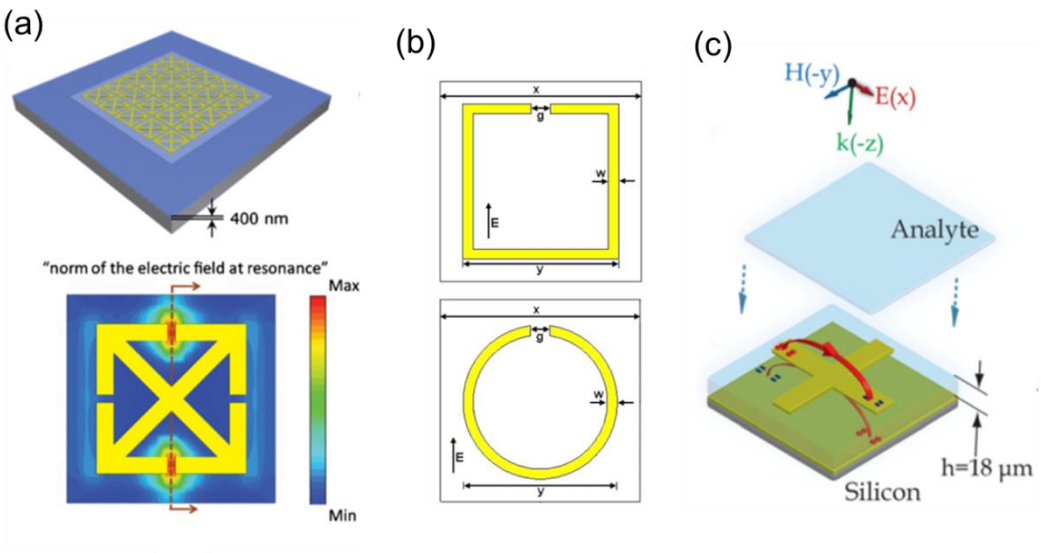

Figure 3.9. Schematic of designs presented in other Works: panel (a) extracted from Ref. [25], panel (b) extracted from Ref. [26], and panel (c) extracted from Ref. [30].

	Analyte Permittivity	Sensitivity (max.)	FOM (max) [nm^{-1}]
Ref. [30]	2.56	4	-
Ref. [25]	3.61	80	-
Ref. [26]	2	3	118
This work	4	578	3558

Table 5. Comparison of different values of sensitivity and FOM achieved in different works, calculated as $S = \Delta\lambda/h_a$ and FOM = S/FWHM. FOM could not be obtained in some cases due to the impossibility of extracting the FWHM from the plots.

To perform a more detailed comparison between these works, we use two alternative sensitivity definitions of the sensor, as specified in Ref. [25] and Ref. [30] $S1 = \Delta f(\%)/(n_a h_a)$, and $S2 = \Delta f(\%)/h_a$. Here, $\Delta f\ (\%) = 100(f_a - f_0) / f_0$ with f_a the resonance frequency at each ha and f_0 the resonance frequency without the analyte, $n_a = \sqrt{\varepsilon_a}$ is the analyte refractive index and h_a is the analyte thickness. With these definitions, it is possible to compare sensors of alternative designs operating in different spectral bands, and using analytes with varied electromagnetic properties. The results of sensitivity comparison are given in Table 6. As can be observed, our results still are better than those obtained in other works, even using other sensitivity definitions.

	Sensitivity #1 (max.) [$\%nm^{-1}$]	Sensitivity #2 (max.) [$\%nm^{-1}$]
Ref. [30]	5.07×10^{-4}	1.01×10^{-3}
Ref. [25]	6.76×10^{-3}	1.28×10^{-2}
Ref. [26]	3.88×10^{-4}	7.75×10^{-4}
This work	1.29×10^{-2}	1.76×10^{-2}

Table 6. Comparison for different values of sensitivity and in different works, where $S\#1 = \Delta f(\%)/\Delta n \cdot h_a$ [nm^{-1}], and $S\#2 = \Delta f(\%)/h_a$ [nm^{-1}].

Performance with lower permittivity

Note that in the studies that can be found in the literature, the analyte typically has a relatively low permittivity (see Table 5), in contrast with our study where $\varepsilon_a \cong 4$. This may be one of the reasons why our sensitivity and FOM results are so high in comparison with the state-of-the-art. To perform a fairer comparison with previous works, a simulation analysis using an analyte of lower permittivity: ε = 2.56 (n = 1.6) was done using our designed structure. In Figure 3.11 (a) is plotted the metasurface reflectivity as the analyte thickness varies from h_a = 100 nm to h_a = 400 nm, with a step of 50 nm. Derived from these results, the relative wavelength shift versus the analyte thickness is displayed in panel (b). With these conditions, a maximum frequency shift of 3.3 GHz is achieved, as shown in Table 7. We calculate the sensitivity and FOM following the same method of the main section of this chapter ($S = \Delta\lambda/h_a$ and FOM = S/FWHM). With these numbers, we obtain the maximum sensitivity value of 184 and FOM of 1322 nm^{-1} for h_a = 100 nm. As we can see, these values are still quite higher than those found in the other works.

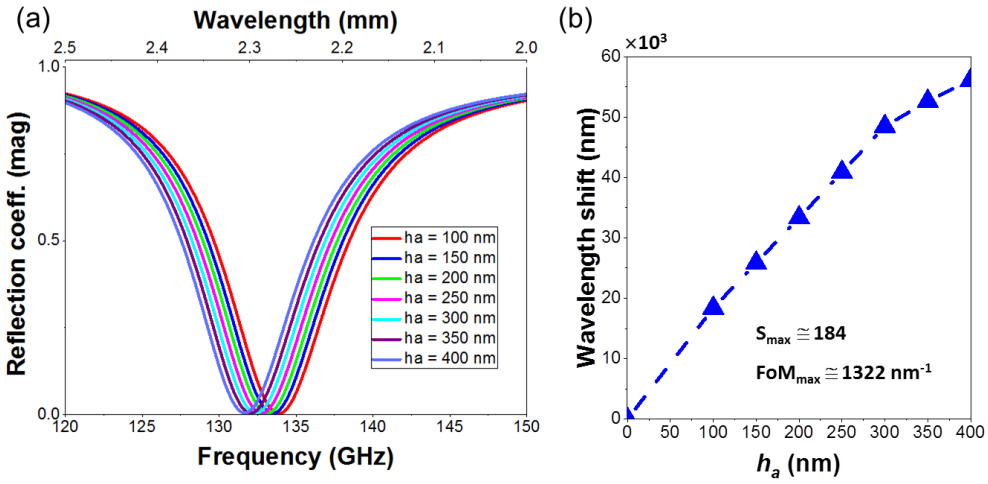

Figure 3.10. (a) Simulated reflection coefficient of the labyrinth metasurface absorber under normal incidence for an analyte with permittivity ε_a = 2.56 and different analyte thicknesses. (b) Wavelength shift as a function of the analyte thickness for extremely thin analytes, calculated as $\Delta\lambda = \lambda_a - \lambda_0$, with λ_a the resonance wavelength at each h_a and λ_0 the resonance wavelength without the analyte.

h_a (nm)	f_{res} (GHz)	λ_{res} (mm)	Δf (GHz)	$\Delta\lambda$(μm)
0	134.5	2.230	0	0
100	133.4	2.249	18.39	1.1
150	132.96	2.256	25.83	1.54
200	132.52	2.264	33.33	1.98
250	132.08	2.271	40.87	2.42
300	131.64	2.279	48.46	2.86
350	131.4	2.283	52.62	3.1
400	131.2	2.287	56.10	3.3

Table 7. Behaviour of the metasurface presented for an analyte with permittivity ε_a = 2.56 and different analyte thicknesses.

3.2. Hole array structures. EOT

In this section various hole array metasurface sensors operating at the THz regime, and a comparison between the regular and anomalous EOT, are presented. The high field intensity that arises near the subwavelength apertures at the EOT resonance is particularly well-suited for sensing applications, since the characteristics of substances placed near the hole array can shift strongly the resonance frequency. Two polarizations are used in the study: parallel to the large period of the structure (d_y), which corresponds to the regular EOT resonance excitation; and parallel to the short period of the metasurface (d_x), which, under the appropriate conditions gives rise to the anomalous EOT resonance. The aim with this strategy is to have a case very far away from supporting the anomalous EOT resonance and another structure very near the condition, so that a small change provoked by an analyte substance can give rise to the anomalous EOT peak.

The performance is then quantitatively evaluated by depositing thin layers of a dielectric analyte on the structures, to obtain both the sensitivity and the FOM. The study concludes with a quantitatively comparison of the results obtained using the regular and anomalous EOT resonance regimes and demonstrate that the optimal case is when we use anomalous EOT and deposition on the non-patterned side.

Design of the empty structure

As shown in the unit cell representation of Figure 3.12 (a), the metasurfaces studied in this work consist of a periodic array of circular holes etched on an aluminum layer of thickness t = 0.5 μm and conductivity $\sigma = 1.5\times10^7$ S/m (note that the nominal conductivity of aluminum is reduced due to roughness), laying on a polypropylene (PP)

slab with permittivity $\varepsilon_{PP} = 2.25$, delta tangent factor $tan\delta \approx 1\times10^{-3}$ and two different thicknesses $h_{PP} = 50$ and 75 µm. The relevant dimensions of the unit cell are $d_x = 115.5$ µm, $d_y = 350$ µm and hole diameter $a = 105$ µm. Two polarizations are used in the study: parallel to the large period of the structure (d_y), which corresponds to the regular EOT resonance excitation [37]; and parallel to the short period of the metasurface (d_x), which, under the appropriate conditions, gives rise to the anomalous EOT resonance [45], [48], [77]. The sensing performance of the metasurfaces is evaluated by depositing a photoresist material of variable thickness (from 3 µm to 13 µm) on them, either on the PP or the HA side. Its complex permittivity is plotted in Figure 3.12 (d).

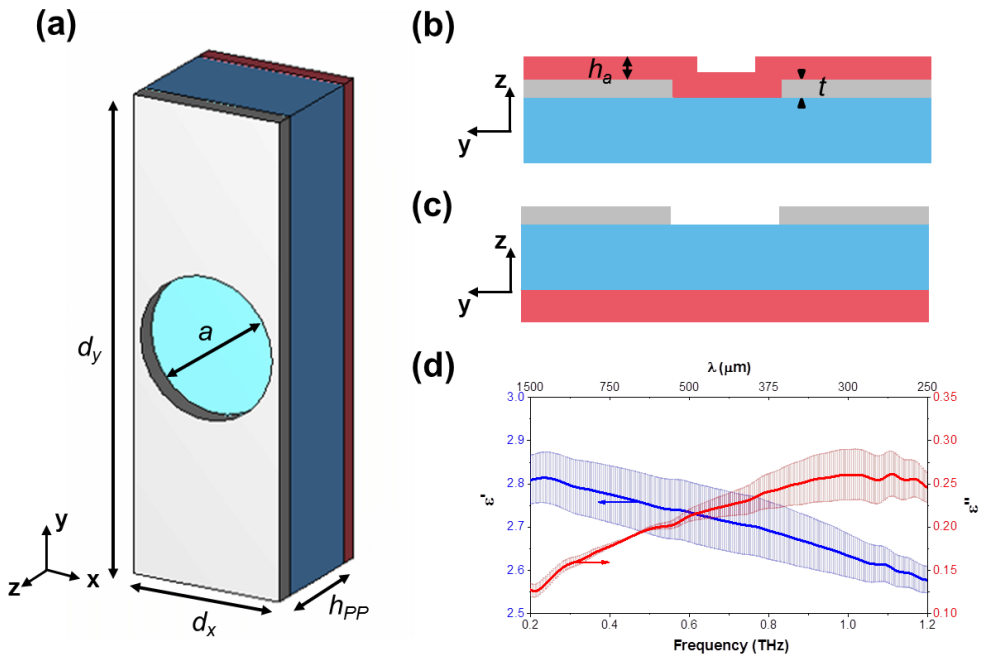

Figure 3.11. (a) Front view and (b), (c) cross-section of the metasurface unit cell, showing the metallization (gray), PP substrate (blue) and analyte (red). Deposition of the analyte is done on the HA (b) and PP (c) faces. Dimensions: $d_x = 115.5$ µm, $d_y = 350$ µm, $a = 105$ µm, $h_{PP} = 50$; 75 µm, $t = 0.5$ µm, $h_a = 3$; 7; 10; 13 µm. (d) Measured frequency response of the complex analyte permittivity, with error bars: real (blue, left axis) and imaginary (red, right axis) components.

Comparing regular and anomalous EOT

Before characterizing the sensing performance of the fabricated HA metasurface, the study begins by analyzing the response of an ideal lossless structure. Thus, the metallic parts are modelled as perfect electric conductors with zero thickness and all dielectric materials are described only by a non-dispersive real permittivity with values $\varepsilon_{PP} = 2.25$ and $\varepsilon_a = 2.65$. Both vertical and horizontal polarizations are considered in order to excite regular and anomalous EOT, respectively, and ascertain which of the two options offers the best results for sensing purposes. As discussed in [45], [48], and explained in the introduction chapter, the appearance of the anomalous EOT depends on the dielectric slab characteristics (h_{PP} and ε_{PP}) as well as the large HA periodicity, d_y. More specifically, the anomalous EOT resonance cutoff can be calculated with the auxiliary factor $F = h_{PP}\sqrt{(\varepsilon_{PP}-1)}/d_y$, so that if $F \geq 0.25$, the anomalous EOT peak will appear. In this initial study the thickness of the PP substrate is fixed to the value $h_{PP} = 78.25$ μm so that $F = 0.25$ and hence the anomalous EOT is exactly at cutoff. On the other hand, the regular EOT resonance exists even in absence of a dielectric substrate, so for this study just a free-standing structure without PP substrate is considered. As shown in Figure 3.13 (a) and (b) (black line) in absence of analyte, the regular EOT resonance takes place at 0.81 THz, whereas the anomalous EOT resonance occurs at 0.84 THz. To evaluate the performance of each resonance in label-free thin-film sensing applications, a dielectric slab acting as analyte with permittivity $\varepsilon_a = 2.65$ and thickness ranging from $h_a = 3$ μm ($8.5\times10-^{3}\lambda_0$, where λ_0 is ~0.35 mm) to 15 μm ($42.9\times10^{-3}\lambda_0$) with a step of 3 μm is added on top. In the anomalous EOT study, the analyte is put on external face of the PP substrate, whereas, obviously, in the regular EOT case (free-standing) the analyte touches the holey metal. As the analyte thickness

increases, the transmission peak redshifts for both resonances, see Figure 3.13.

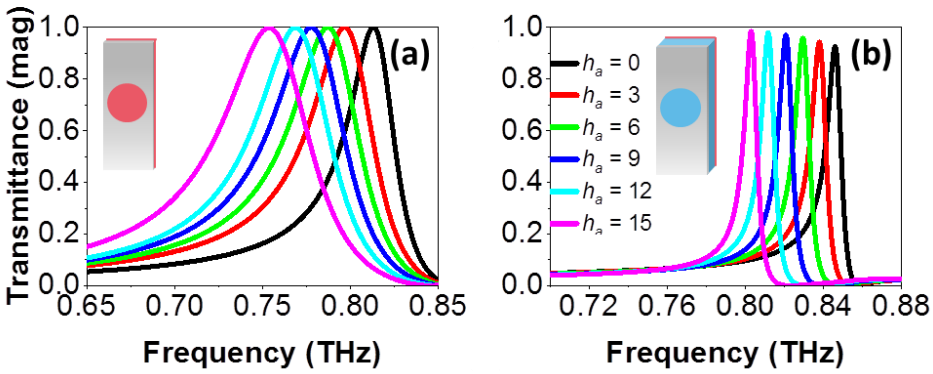

Figure 3.12. Transmission coefficient for the regular EOT (a) and anomalous EOT (b) of the structure under study.

To have a quantitative assessment of the behavior, the wavelength shift is plotted as a function of h_a in Figure 3.13 panels (a) and (b). Comparing both plots, and looking at the results in the Table 8, it is clear that the shift is stronger for the regular resonance, suggesting at first sight that this regime is more appropriate for sensing purposes. Nevertheless, to clarify this aspect a formal evaluation of the performance in terms of sensitivity and FOM is carried out and represented in Figure 3.14. The average sensitivity is equal to the slope of the regression lines in panels (a) and (b), and the FOM is shown in panels (c) and (d). With these values, we find that the regular EOT configuration is slightly better than the anomalous EOT in terms of average sensitivity: 2.04 vs. 1.19. However, the FOM shows that the anomalous EOT is clearly superior to the regular EOT resonance, with an average value of 153.7 mm^{-1}. This is much higher than the value of 45.4 mm^{-1} calculated for the latter and is due to the comparatively narrower FWHM of the anomalous EOT resonance. With these results, it can be affirmed the anomalous EOT presents a better behavior for sensing purposes than the regular EOT, improving the FOM by a factor of more than 3.

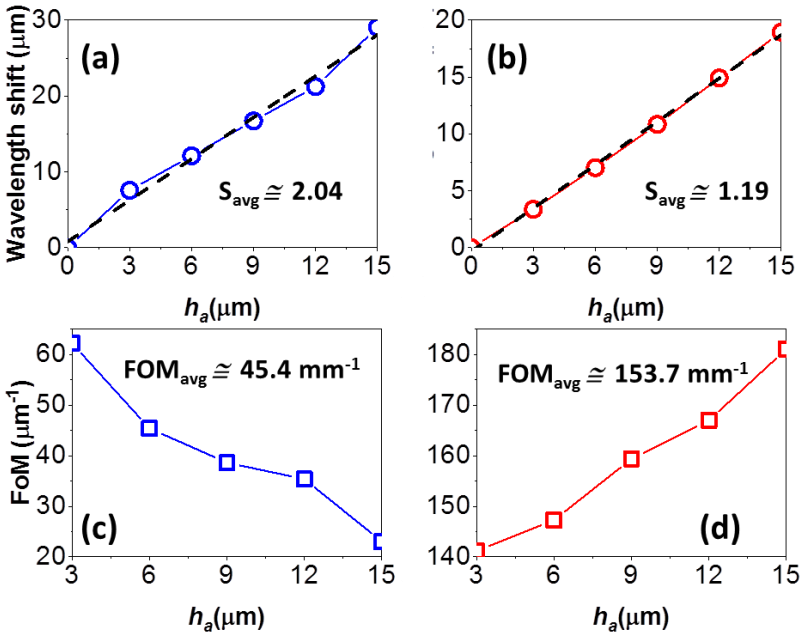

Figure 3.13. (a) Wavelength shift as a function of the analyte thickness for extremely thin analytes, for the regular EOT resonance, calculated as $\Delta\lambda = \lambda_a - \lambda_0$, with λ_a the resonance wavelength at each h_a and λ_0 the resonance wavelength without the analyte. (b) Idem for the anomalous EOT. FOM as a function of the analyte thickness, for the regular EOT (c) and for the anomalous EOT (d).

	h_a (μm)	Δf (GHz)	Δλ(μm)	S	FOM (mm^{-1})
Regular EOT	0	0	0	-	-
	3	16.35	7.574	2.52	62.25
	6	25.85	12.120	2.02	45.42
	9	35.25	16.726	1.86	38.65
	12	44.25	21.243	1.77	35.37
	15	59.35	29.063	1.94	23.03
Anomalos EOT	0	0	0	-	-
	3	8	3.387	1.13	141.16
	6	16.45	7.034	1.17	147.28
	9	25.1	10.847	1.21	159.40
	12	34.15	14.922	1.24	166.99
	15	42.9	18.949	1.26	181.11

Table 8. Behavior of the simulated metasurface for different analyte thicknesses. Regular and anomalous EOT results.

Designed Hole Array sensor

After this initial study, we concentrate now on the analysis of the designed and fabricated HA metasurfaces. As the aim here is to evaluate in depth the performance of the anomalous EOT resonance as a sensing platform, two different substrate thicknesses are used h_{PP} = 75 μm (Figure 3.15) and h_{PP} = 50 μm (Figure 3.16), that correspond to F = 0.24 and 0.16, respectively. The first case is chosen to have the anomalous resonance very near cutoff, so that a slight change provoked by an analyte can give rise to a strong spectral variation. Conversely, in the second case the anomalous EOT resonance is deeply in cutoff and we do not expect a sharp response, at least with thin analytes. The sensing performance of the structures is evaluated by depositing four different analyte thicknesses: h_a = 3 μm ($8.5\times10^{-3}\lambda_0$,); 7 μm ($19.8\times10^{-3}\lambda_0$); 10 μm ($28.3\times10^{-3}\lambda_0$); and 13 μm ($36.8\times10^{-3}\lambda_0$). Numerical results are shown in the upper panels (a), (b), (e), (f); and experimental measurements on the lower panels (c), (d), (g), (h) of Figures 3.15 and 3.16. To have a complete picture of the performance, two different scenarios were considered: analyte deposited on the HA side and on the PP side, schematically depicted in Figure 3.12(b) and (c).

Focusing first on the horizontal polarization (anomalous EOT), we find that the transmission coefficient without analyte (h_a = 0) shows in all considered cases clear resonant features at ~0.85 THz, with a very good agreement between simulation and measurement, see black curves in Figure 3.15. Although in the case of the 75 μm thick PP film [Figure 3.15 (a)-(d)] the anomalous EOT resonance is slightly below cutoff, it is close enough so that it gives rise to a high transmission peak followed by a null in the spectrum. This is in contrast with the behavior of the 50 μm thick PP film [Figure 3.15 (e)-(h)] that shows only a local maximum (a "kink") with reduced amplitude (~0.5), as

expected [45], [48], [77]. Now, as the analyte thickness increases, the optimal scenario is when the analyte is deposited on the PP side of the h_{PP} = 75 μm thick metasurface [Figure 3.15 (a), (c)], with an average sensitivity of ~0.8 (~1.24) and an average FOM of ~28.6 mm^{-1} (~46 mm^{-1}) in the experimental (numerical) results. This is in agreement with our analysis above, since depositing on the PP side is equivalent to increasing the dielectric thickness (as a side comment, note that the peak amplitude decreases as h_a increases due to the growing ohmic loss because, unlike the previous study, we are considering here a lossy and dispersive analyte. Note also that this effect is more evident in the simulation than in the experimental results, probably because in the experiment the characteristics of the analyte might differ between successive depositions and, in addition, it is rather difficult to have a proper characterization of metal and dielectric losses). When the analyte is deposited on the HA side [Figure 3.15 (b), (d)] the frequency shift of the anomalous EOT resonance is negligible, rendering this configuration ineffective for sensing purposes. As explained in [45], two different anomalous EOT peaks can be excited independently by placing dielectric slabs on both sides of the holey metal, if this metal is thick enough. In the configuration considered here, the analyte slab is too thin and hence unable to excite its own anomalous EOT resonance (i.e. $F << 0.25$ in that side). This is why in the spectral response we only see the peak corresponding to the PP slab, which is largely insensitive to the analyte deposition on the other face.

For the 50 μm PP thick structure with analyte deposited on the PP side we find that the "kink" becomes narrower and its amplitude grows faintly as h_a is enlarged, see Figure 3.15 (e), (g). This is because we are approaching gradually, but never reaching cutoff, even with the largest analyte thickness. In practice, this means that it might be feasible to perform sensing by looking at the peak amplitude variation. At least in

simulation [Figure 3.15 (e)] this looks viable, but it seems virtually impossible in the experiment [Figure 3.15 (g)], probably due to fabrication tolerances, and the growing Q factor of the resonance that increases ohmic loss. When the analyte is placed on the HA side [Figure 3.15 (f), (h)] we notice a negligible frequency shift but, interestingly, a clear amplitude increment of the kink. This enhancement in the transmission coefficient is associated with a better impedance matching of the structure. From the specialized literature [70], it is known that the optimal operation of frequency selective surfaces and spatial filters is achieved when both faces of the metallic film are coated with dielectric slabs of identical characteristics. In this case, increasing the analyte thickness leads to a better matching of the impedance seen at both interfaces, giving as a result a higher peak amplitude. This way, it is possible to define a new sensitivity, referred to as Amplitude Sensitivity (AS) and calculated as the ratio between the variation of the amplitude at the resonant frequency and the variation of the analyte thickness: AS = $\Delta A/h_a$. With this definition, we get experimentally AS = 0.02 μm^{-1}. Note that in this case it is impossible to define a FOM, due to the inexistence of a valid FWHM.

Next, vertical polarization (regular EOT) is considered, just for comparison purposes, see all results in Figure 3.16. In this case, the response is very similar regardless the PP thickness, as this parameter is not critical for the performance (in contrast to anomalous EOT). Therefore, we will study both cases, h_{pp} = 50 and 75 μm, in parallel. The first difference we observe in the spectral response in comparison with the previous study is that there are two resonance peaks, at 690 and 847 GHz. Each peak is related with the EOT resonance principally at the PP and air interfaces [78]. Therefore, depositing the analyte on the PP side mainly shifts the low frequency peak and depositing on the air side mainly shifts the high frequency peak. Although in the simulation both peaks can be potentially employed for sensing purposes, in the

measurement only the low frequency resonance presents noticeable shift. Furthermore, the structure with h_{pp} = 50 µm has a better performance in practice, probably due to the thinner substrate, which is further from the saturation point of the maximum achievable frequency shift. Consequently, we only select the cases highlighted with a dotted circle for the calculation of the sensitivity and FOM as these are the ones in which we can appreciate a frequency shift enough to use the structure as a sensing device, and we have a good agreement between the simulated and measured results. Note that in the case of the second resonance when depositing on the HA side, the FOM cannot be calculated due to the low magnitude of the peak.

To ease the comparison, all the values of the cases of interest extracted from the experimental measurements are collected in Table 9. As shown there, although the sensitivity in the anomalous EOT case is below the regular EOT case, the FOM is much higher in agreement with our initial study.

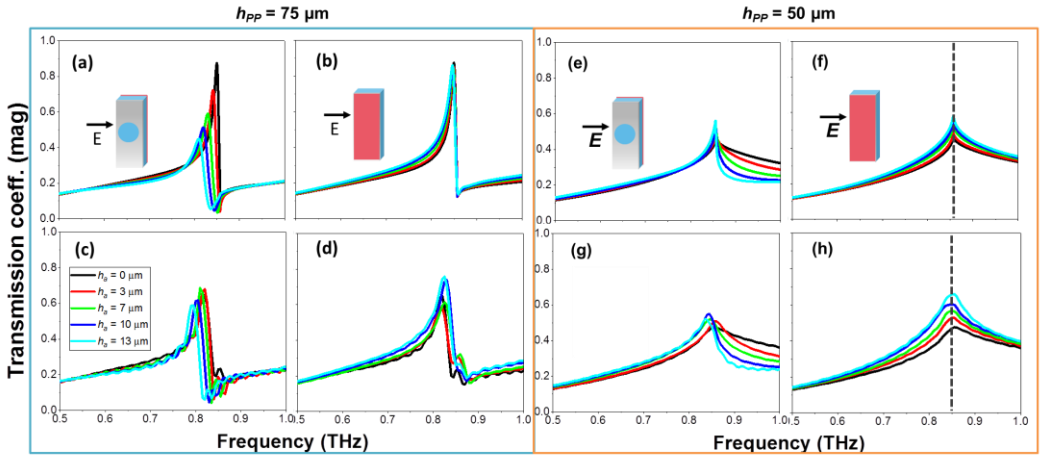

Figure 3.14. Transmission coefficient magnitude at the anomalous EOT regime in HA metasurfaces with h_{pp} = 75 µm (a)-(d) and h_{pp} = 50 µm (e)-(f) µm under normal incidence and different analyte thicknesses: h_a = 3 µm (red); 7 µm (green); 10 µm (dark blue); 13 µm (cyan). Simulated (top) and measured (bottom) results.

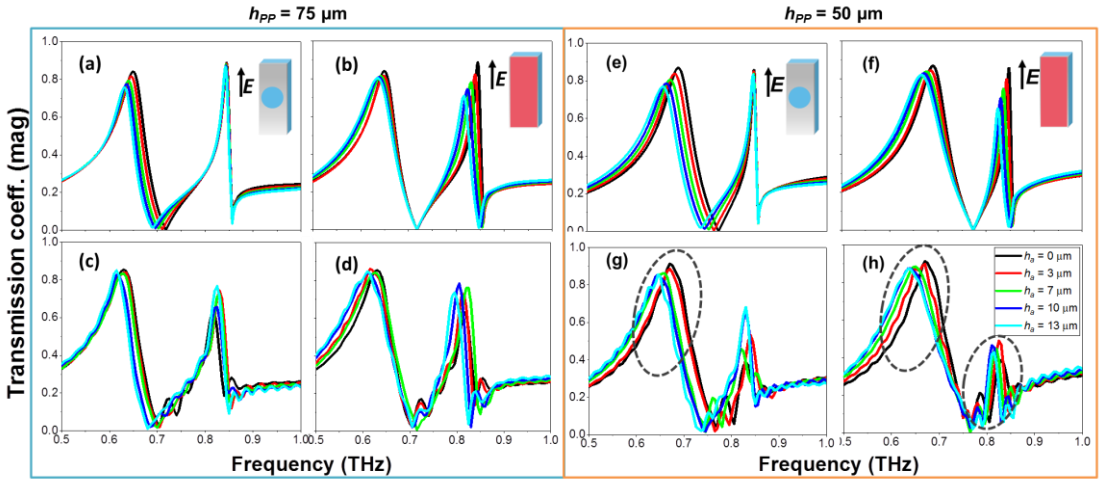

Figure 3.15. Transmission coefficient magnitude at the regular EOT regime in HA metasurfaces with h_{pp} = 75 µm (a)-(d) and h_{pp} = 50 µm (e)-(f) µm under normal incidence and different analyte thicknesses: h_a = 3 µm (red); 7 µm (green); 10 µm (dark blue); 13 µm (cyan) for the anomalous EOT. Simulated (top) and measured (bottom) results.

Resonance	h_{pp} (µm)	Analyte side	S	FOM (mm^{-1})
Anomalous	75	PP	0.8	28.6
		HA	–	–
	50	PP	-	–
		HA	0.02 $µm^{-1}$ *	–
Regular	75	PP	–	–
		HA	–	–
	50	PP	1.2	12.9
		HA	1.85/0.68 **	16.6/–

Table 9. Comparison of different values of average sensitivity and FOM achieved in the different configurations shown in Figures 3 and 4, experimental results. *Note that in this cases we are referring to the amplitude sensitivity, AS = $\Delta A/h_a$.**The first/second number refers to the first/second resonance

Conclusions and future work

Conclusions

- In this work, we have demonstrated that sensing in the THz region using metasurfaces provides interesting results. Two different structures have been designed, manufactured, and studied and we have proved the good sensing performance, improving the previous results found in the literature.

- We have reported here a labyrinth metasurface which operates in the near-to-unity absorptivity regime at the low-frequency edge of the THz spectrum and exhibits extreme FOM and sensitivity to thin film detection, exceeding largely the results found in the literature by a factor of 30, if we compare our work with similar structures.

- The metasurface sensor investigated in this work operates at relatively long waves ($\lambda_0 \sim 2.2$ mm) that potentially allows one to employ more compact and less expensive field-oriented millimetre-wave instrumentation than it is required for higher-frequency THz spectral measurements. We foresee these results as a proof-of-concept that could be extended in the future to biological sensing, where thin-film samples become essential.

- We have demonstrated the superior performance of a HA metasurface when it operates at the anomalous EOT resonance, exceeding largely the results obtained at the regular EOT in label-free thin-film sensing applications. Although the frequency shift and hence the sensitivity of the anomalous EOT resonance is smaller than those of the regular EOT resonance, its comparatively narrower FWHM leads to an increment of the FOM.

- Two HA metasurfaces of different PP thicknesses have been fabricated and measured to analyze the effects on the sensing quality parameters depending on the side in which we deposit the analyte under measurement. We have demonstrated that, for thick enough substrates, sensing in the anomalous EOT and depositing on the non-patterned side of the metasurface is a much better option with lower sensitivity but a higher FOM magnitude and brings the additional advantage that in routine operation the structure can be cleaned without damaging the metallic pattern.

- Additionally, we have found an alternative for thin-film sensing based on a variation of amplitude. This can be used when the substrate thickness is too thin to exhibit the anomalous EOT peak and takes place when the analyte is deposited on the patterned side of the metasurface. These results demonstrate the excellent performance of the anomalous EOT resonance in practical thin-film sensing platforms.

Future work

As future work, it would be interesting realize biological sensing using designed devices. The proposed approach constitutes an important step toward the fabrication of high sensitivity thin film sensors and could be extrapolated towards biosensors able to detect biological samples such as bacteria, proteins, or DNA, among others.

Although the labyrinths have turned out to have an interesting geometry to perform sensing, there are many other geometries that could be used to create new devices. This is the case of the so-called space filling curves, such as those of Peano or Hilbert, or fractal structures.

References

[1] P. H. Siegel, “Terahertz technology,” *IEEE Trans. Microw. Theory Tech.*, vol. 50, no. 3, pp. 910–928, Mar. 2002.

[2] Y. J. Ding, “Progress in terahertz sources based on difference-frequency generation [Invited],” *J. Opt. Soc. Am. B*, vol. 31, no. 11, p. 2696, 2014.

[3] T. Noguchi, A. Ueda, H. Iwashita, S. Takano, Y. Sekimoto, M. Ishiguro, T. Ishibashi, H. Ito, and T. Nagatsuma, “Millimeter Wave Generation Using a Uni-Traveling-Carrier Photodiode,” *12th Int. Symp. Sp. Terahertz Technol.*, pp. 73–80, 2001.

[4] J. H. Smet, C. G. Fonstad, and Q. Hu, “Intrawell and interwell intersubband transitions in multiple quantum wells for far-infrared sources,” *J. Appl. Phys.*, vol. 79, no. 12, pp. 9305–9320, 1996.

[5] K. Saito, T. Tanabe, and Y. Oyama, “Design of a terahertz parametric oscillator based on a resonant cavity in a terahertz waveguide,” *J. Appl. Phys.*, vol. 116, no. 4, 43108, 2014.

[6] P. E. L. Iu, F. Q. I. Eng, W. L. I. Eifan, Y. E. W. Ang, Z. H. L. Iu, H. W. U. Ongming, W. E. I. N. Ing, W. E. I. S. Hi, and J. I. Y. Ao, “Low-threshold terahertz-wave generation based on a cavity phase-matched parametric process in a Fabry – Perot microresonator,” vol. 35, no. 1, pp. 68–72, 2018.

[7] D. Saeedkia, *Handbook of terahertz technology for imaging, sensing and communications*. WP Woodhead Publishing, 2013.

[8] S. S. Dhillon, M. S. Vitiello, E. H. Linfield, A. G. Davies, M. C. Hoffmann, J. Booske, C. Paoloni, M. Gensch, P. Weightman, G. P. Williams, E. Castro-Camus, D. R. S. Cumming, F. Simoens, I. Escorcia-Carranza, J. Grant, S. Lucyszyn, M. Kuwata-Gonokami, K. Konishi, M. Koch, C. A. Schmuttenmaer, T. L. Cocker, R. Huber, A. G. Markelz, Z. D. Taylor, V. P. Wallace, J. Axel Zeitler, J. Sibik, T. M. Korter, B. Ellison, S. Rea, P. Goldsmith, K. B. Cooper, R. Appleby, D. Pardo, P. G. Huggard, V. Krozer, H. Shams, M. Fice, C. Renaud, A.

Seeds, A. Stöhr, M. Naftaly, N. Ridler, R. Clarke, J. E. Cunningham, and M. B. Johnston, “The 2017 terahertz science and technology roadmap,” *J. Phys. D. Appl. Phys.*, vol. 50, no. 4, p. 43001, Feb. 2017.

[9] C. Debus and P. H. Bolivar, “Frequency selective surfaces for high sensitivity terahertz sensing,” *Appl. Phys. Lett.*, vol. 91, no. 18, pp. 2005–2008, 2007.

[10] B. Ng, J. Wu, S. M. Hanham, A. I. Fernández-Domínguez, N. Klein, Y. F. Liew, M. B. H. Breese, M. Hong, and S. A. Maier, “Spoof Plasmon Surfaces: A Novel Platform for THz Sensing,” *Adv. Opt. Mater.*, vol. 1, no. 8, pp. 543–548, Aug. 2013.

[11] T. Driscoll, G. O. Andreev, D. N. Basov, S. Palit, S. Y. Cho, N. M. Jokerst, and D. R. Smith, “Tuned permeability in terahertz split-ring resonators for devices and sensors,” *Appl. Phys. Lett.*, vol. 91, no. 6, pp. 3–5, 2007.

[12] J. F. O’Hara, W. Withayachumnankul, and I. A. I. Al-Naib, “A review on thin-film sensing with terahertz waves,” *J. Infrared, Millimeter, Terahertz Waves*, vol. 33, no. 3, pp. 245–291, 2012.

[13] V. G. Veselago, “The electrodynamics of substances with simultaneously negative values of ε and μ,” *Sov. Phys. Uspekhi*, vol. 10, no. 4, 1968.

[14] J. A. Porto and F. J. Garcıa, “Transmission Resonances on Metallic Gratings with Very Narrow Slits,” pp. 2845–2848, 1999.

[15] D. R. Smith, D. R. Smith, W. J. Padilla, W. J. Padilla, D. C. Vier, D. C. Vier, S. C. Nemat-Nasser, S. C. Nemat-Nasser, S. Schultz, and S. Schultz, “Composite Medium with Simultaneously Negative Permeability and Permittivity,” *Phys. Rev. Lett.*, vol. 84, no. 18, pp. 4184–4187, 2000.

[16] J. B. Pendry, D. Schurig, and D. R. Smith, “Controlling electromagnetic fields.,” *Science*, vol. 312, no. 5781, pp. 1780–1782, Jun. 2006.

[17] D. Schurig, J. J. Mock, B. J. Justice, S. A. Cummer, J. B. Pendry, A. F. Starr, and D. R. Smith, “Metamaterial electromagnetic cloak at microwave frequencies,” *Science*, vol. 314, no. 5801, pp. 977–980, 2006.

[18] L. Huang, X. Chen, H. Mühlenbernd, H. Zhang, S. Chen, B. Bai, Q. Tan, G. Jin,

K. W. Cheah, C. W. Qiu, J. Li, T. Zentgraf, and S. Zhang, “Three-dimensional optical holography using a plasmonic metasurface,” *Nat. Commun.*, vol. 4, no. May, pp. 1–8, 2013.

[19] M. Gharghi, C. Gladden, T. Zentgraf, Y. Liu, X. Yin, J. Valentine, and X. Zhang, “A carpet cloak for visible light,” *Nano Lett.*, vol. 11, no. 7, pp. 2825–2828, 2011.

[20] B. Orazbayev, N. Mohammadi Estakhri, A. Alù, and M. Beruete, “Experimental Demonstration of Metasurface-Based Ultrathin Carpet Cloaks for Millimeter Waves,” *Adv. Opt. Mater.*, vol. 5, no. 1, p. 1600606, Jan. 2017.

[21] R. Yahiaoui, S. Tan, L. Cong, R. Singh, F. Yan, and W. Zhang, “Multispectral terahertz sensing with highly flexible ultrathin metamaterial absorber,” *J. Appl. Phys.*, vol. 118, no. 8, p. 83103, Aug. 2015.

[22] P. Rodríguez-Ulibarri, S. A. Kuznetsov, and M. Beruete, “Wide angle terahertz sensing with a cross-dipole frequency selective surface,” *Appl. Phys. Lett.*, vol. 108, 2016.

[23] S. Y. Chiam, R. Singh, J. Gu, J. Han, W. Zhang, and A. A. Bettiol, “Increased frequency shifts in high aspect ratio terahertz split ring resonators,” *Appl. Phys. Lett.*, vol. 94, no. 6, pp. 18–20, 2009.

[24] S. Y. Chiam, R. Singh, W. Zhang, and A. A. Bettiol, “Controlling metamaterial resonances via dielectric and aspect ratio effects,” *Appl. Phys. Lett.*, vol. 97, no. 19, pp. 2–4, 2010.

[25] H. Tao, A. C. Strikwerda, M. Liu, J. P. Mondia, E. Ekmekci, K. Fan, D. L. Kaplan, W. J. Padilla, X. Zhang, R. D. Averitt, and F. G. Omenetto, “Performance enhancement of terahertz metamaterials on ultrathin substrates for sensing applications,” *Appl. Phys. Lett.*, vol. 97, no. 26, p. 261909, 2010.

[26] C. Sabah and H. G. Roskos, “Terahertz sensing application by using planar split-ring-resonator structures,” *Microsyst. Technol.*, vol. 18, no. 12, pp. 2071–2076, 2012.

[27] D.-K. Lee, J.-H. Kang, J.-S. Lee, H.-S. Kim, C. Kim, J. Hun Kim, T. Lee, J.-H.

Son, Q.-H. Park, and M. Seo, “Highly sensitive and selective sugar detection by terahertz nano-antennas,” *Sci. Rep.*, vol. 5, p. 15459, 2015.

[28] W. Withayachumnankul, H. Lin, K. Serita, C. M. Shah, S. Sriram, M. Bhaskaran, M. Tonouchi, C. Fumeaux, and D. Abbott, “Sub-diffraction thin-film sensing with planar terahertz metamaterials,” *Opt. Express*, vol. 20, no. 3, pp. 3345–3352, 2012.

[29] L. Xie, W. Gao, J. Shu, Y. Ying, and J. Kono, “Extraordinary sensitivity enhancement by metasurfaces in terahertz detection of antibiotics.,” *Sci. Rep.*, vol. 5, p. 8671, 2015.

[30] L. Cong, S. Tan, R. Yahiaoui, F. Yan, W. Zhang, and R. Singh, “Experimental demonstration of ultrasensitive sensing with terahertz metamaterial absorbers: A comparison with the metasurfaces,” *Appl. Phys. Lett.*, vol. 106, no. 3, p. 31107, Jan. 2015.

[31] I. Jauregui, M. Beruete, and P. Rodriguez-ulibarri, “Design of terahertz sensors based on metasurfaces for fungal infection detection,” 2016.

[32] T. W. Ebbesen, H. J. Lezec, H. F. Ghaemi, T. Thio, and P. A. Wolff, “Extraordinary optical transmission through sub-wavelength hole arrays,” *Nature*, vol. 391, pp. 667–669, Feb. 1998.

[33] I. Avrutsky, Y. Zhao, and V. Kochergin, “Surface-plasmon-assisted resonant tunneling of light through a periodically corrugated thin metal film.,” *Opt. Lett.*, vol. 25, no. 9, pp. 595–597, 2000.

[34] L. Martín-Moreno, F. J. García-Vidal, H. J. Lezec, K. M. Pellerin, T. Thio, J. B. Pendry, and T. W. Ebbesen, “Theory of Extraordinary Optical Transmission through Subwavelength Hole Arrays,” *Phys. Rev. Lett.*, vol. 86, no. 6, pp. 1114–1117, Feb. 2001.

[35] F. J. Garcia-Vidal, L. Martin-Moreno, T. W. Ebbesen, and L. Kuipers, “Light passing through subwavelength apertures,” *Rev. Mod. Phys.*, vol. 82, no. 1, pp. 729–787, Mar. 2010.

[36] F. J. García de Abajo, “Colloquium: Light scattering by particle and hole arrays,”

Rev. Mod. Phys., vol. 79, no. 4, pp. 1267–1290, Oct. 2007.

[37] M. Beruete, M. Sorolla, I. Campillo, J. S. Dolado, L. Martín-Moreno, J. Bravo-Abad, and F. J. García-Vidal, "Enhanced millimeter-wave transmission through subwavelength hole arrays," *Opt. Lett.*, vol. 29, no. 21, pp. 2500–2502, Nov. 2004.

[38] T. Xu, H. Shi, Y. K. Wu, A. F. Kaplan, J. G. Ok, and L. J. Guo, "Structural colors: From plasmonic to carbon nanostructures," *Small*, vol. 7, no. 22, pp. 3128–3136, 2011.

[39] Y. Zhao, Y. Zhao, S. Hu, J. Lv, Y. Ying, G. Gervinskas, and G. Si, "Artificial Structural Color Pixels: A Review," *Materials (Basel).*, vol. 10, no. 8, p. 944, Aug. 2017.

[40] M. Beruete, M. Sorolla, and I. Campillo, "Left-handed extraordinary optical transmission through a photonic crystal of subwavelength hole arrays," *Opt. Express*, vol. 14, no. 12, pp. 5445–5455, Jun. 2006.

[41] M. Navarro-Cía, M. Beruete, M. Sorolla, and I. Campillo, "Negative refraction in a prism made of stacked subwavelength hole arrays," *Opt. Express*, vol. 16, no. 2, pp. 560–566, Jan. 2008.

[42] J. Valentine, S. Zhang, T. Zentgraf, E. Ulin-Avila, D. A. Genov, G. Bartal, and X. Zhang, "Three-dimensional optical metamaterial with a negative refractive index," *Nature*, vol. 455, no. 7211, pp. 376–379, Sep. 2008.

[43] M. Beruete, M. Sorolla, I. Campillo, J. S. Dolado, L. Martinn-Moreno, J. Bravo-Abad, and F. J. Garcia-Vidal, "Enhanced millimeter wave transmission through quasioptical subwavelength perforated plates," *IEEE Trans. Antennas Propag.*, vol. 53, no. 6, pp. 1897–1903, 2005.

[44] F. Medina, F. Mesa, and R. Marqués, "Extraordinary transmission through arrays of electrically small holes from a circuit theory perspective," *IEEE Trans. Microw. Theory Tech.*, vol. 56, no. 12, pp. 3108–3120, 2008.

[45] M. Beruete, M. Navarro-Cia, and M. Sorolla Ayza, "Understanding Anomalous Extraordinary Transmission From Equivalent Circuit and Grounded Slab

Concepts," *IEEE Trans. Microw. Theory Tech.*, vol. 59, no. 9, pp. 2180–2188, Sep. 2011.

[46] M. Beruete, M. Navarro-Cía, S. A. Kuznetsov, and M. Sorolla, "Circuit approach to the minimal configuration of terahertz anomalous extraordinary transmission," *Appl. Phys. Lett.*, vol. 98, no. 1, pp. 3–5, 2011.

[47] R. W. Wood, "On remarkable case of uneven distribution of light in a diffraction grating spectrum," *Philos. Mag.*, vol. 4, pp. 396–402, 1902.

[48] M. Beruete, M. Navarro-Cía, S. A. Kuznetsov, and M. Sorolla, "Circuit approach to the minimal configuration of terahertz anomalous extraordinary transmission," *Appl. Phys. Lett.*, vol. 98, no. 1, p. 14106, Jan. 2011.

[49] A. G. Brolo, R. Gordon, B. Leathem, and K. L. Kavanagh, "Surface plasmon sensor based on the enhanced light transmission through arrays of nanoholes in gold films," *Langmuir*, vol. 20, no. 12, pp. 4813–4815, 2004.

[50] R. Gordon, D. Sinton, K. L. Kavanagh, and A. G. Brolo, "A New Generation of Sensors Based on Extraordinary Optical Transmission," *Acc. Chem. Res.*, vol. 41, no. 8, pp. 1049–1057, Aug. 2008.

[51] R. Gordon, A. G. Brolo, D. Sinton, and K. L. Kavanagh, "Resonant optical transmission through hole-arrays in metal films: Physics and applications," *Laser Photonics Rev.*, vol. 4, no. 2, pp. 311–335, 2010.

[52] T. Ding, M. Hong, A. M. Richards, T. I. Wong, X. Zhou, and C. L. Drum, "Quantification of a Cardiac Biomarker in Human Serum Using Extraordinary Optical Transmission (EOT)," *PLoS One*, vol. 10, no. 3, p. e0120974, Mar. 2015.

[53] F. Eftekhari, C. Escobedo, J. Ferreira, X. Duan, E. M. Girotto, A. G. Brolo, R. Gordon, and D. Sinton, "Nanoholes As Nanochannels: Flow-through Plasmonic Sensing," *Anal. Chem.*, vol. 81, no. 11, pp. 4308–4311, Jun. 2009.

[54] A. A. Yanik, M. Huang, O. Kamohara, A. Artar, T. W. Geisbert, J. H. Connor, and H. Altug, "An optofluidic nanoplasmonic biosensor for direct detection of live viruses from biological media," *Nano Lett.*, vol. 10, no. 12, pp. 4962–4969, 2010.

[55] J. Chen, F. Gan, Y. Wang, and G. Li, "Plasmonic Sensing and Modulation Based on Fano Resonances," *Adv. Opt. Mater.*, vol. 6, no. 9, pp. 1–21, 2018.

[56] A.-P. Blanchard-Dionne and M. Meunier, "Sensing with periodic nanohole arrays," *Adv. Opt. Photonics*, vol. 9, no. 4, p. 891, 2017.

[57] H. T. Chorsi, Y. Zhu, and J. X. J. Zhang, "Patterned Plasmonic Surfaces—Theory, Fabrication, and Applications in Biosensing," *J. Microelectromechanical Syst.*, vol. 26, no. 4, pp. 718–739, 2017.

[58] C. Escobedo, "On-chip nanohole array based sensing: A review," *Lab Chip*, vol. 13, no. 13, pp. 2445–2463, 2013.

[59] T. Weiland, "A discretization method for the solution of Maxwell's equations for six-component Field," *Int. J. Electron. Commun.*, vol. 31, no. 3, pp. 116–120, 1977.

[60] Q. Wu and X. C. Zhang, "Free-space electro-optics sampling of mid-infrared pulses," *Appl. Phys. Lett.*, vol. 71, no. 10, pp. 1285–1286, 1997.

[61] A. A. Mamrashev and O. I. Potaturkin, "Characteristics of the system of polarization-optical detection of a pulsed terahertz spectrometer," *Optoelectron. Instrum. Data Process.*, vol. 47, no. 4, pp. 332–337, 2011.

[62] M. Navarro-Cia, S. A. Kuznetsov, M. Aznabet, M. Beruete, F. Falcone, and M. S. Ayza, "Route for bulk millimeter wave and terahertz metamaterial design," *IEEE J. Quantum Electron.*, vol. 47, no. 3, pp. 375–385, Mar. 2011.

[63] H. Wasa, K., Kanno, I., Kotera, *Handbook of Sputter Deposition Technology*, (Second Ed. Elsevier Inc., 2012.

[64] S. A. Kuznetsov, A. G. Paulish, M. Navarro-Cía, and A. V. Arzhannikov, "Selective Pyroelectric Detection of Millimetre Waves Using Ultra-Thin Metasurface Absorbers," *Sci. Rep.*, vol. 6, no. 1, p. 21079, Aug. 2016.

[65] J. F. O'Hara, W. Withayachumnankul, and I. Al-Naib, "A Review on Thin-film Sensing with Terahertz Waves," *J. Infrared, Millimeter, Terahertz Waves*, vol. 33, no. 3, pp. 245–291, Mar. 2012.

[66] M. A. Agafonov, A. V. Arzhannikov, N. S. Ginzburg, V. G. Ivanenko, P. V. Kalinin, S. A. Kuznetsov, N. Y. Peskov, and S. L. Sinitsky, "Generation of hundred joules pulses at 4-mm wavelength by FEM with sheet electron beam," *IEEE Trans. Plasma Sci.*, vol. 26, no. 3, pp. 531–535, Jun. 1998.

[67] A. V. Arzhannikov, N. S. Ginzburg, P. V. Kalinin, S. A. Kuznetsov, A. M. Malkin, N. Y. Peskov, A. S. Sergeev, S. L. Sinitsky, V. D. Stepanov, M. Thumm, and V. Y. Zaslavsky, "Using Two-Dimensional Distributed Feedback for Synchronization of Radiation from Two Parallel-Sheet Electron Beams in a Free-Electron Maser," *Phys. Rev. Lett.*, vol. 117, no. 11, p. 114801, 2016.

[68] A. V. Burdakov, A. V. Arzhannikov, V. S. Burmasov, I. A. Ivanov, M. V. Ivantsivsky, I. V. Kandaurov, S. A. Kuznetsov, V. V. Kurkuchekov, K. I. Mekler, S. V. Polosatkin, S. S. Popov, V. V. Postupaev, A. F. Rovenskikh, V. F. Sklyarov, M. K. A. Thumm, Y. A. Trunev, and L. N. Vyacheslavov, "Microwave Generation during 100 keV Electron Beam Relaxation in GOL-3," *Fusion Sci. Technol.*, vol. 63, no. 1T, pp. 286–288, May 2013.

[69] A. V. Arzhannikov, A. V. Burdakov, V. S. Burmasov, D. E. Gavrilenko, I. A. Ivanov, A. A. Kasatov, S. A. Kuznetsov, K. I. Mekler, S. V. Polosatkin, V. V. Postupaev, A. F. Rovenskikh, S. L. Sinitsky, V. F. Sklyarov, and L. N. Vyacheslavov, "Observation of spectral composition and polarization of sub-terahertz emission from dense plasma during relativistic electron beam-plasma interaction," *Phys. Plasmas*, vol. 21, no. 8, p. 82106, Aug. 2014.

[70] B. A. Munk, *Frequency Selective Surfaces: Theory and Design*. Wiley-Interscience, 2000.

[71] F. Costa, A. Monorchio, and G. Manara, "An overview of equivalent circuit modeling techniques of frequency selective surfaces and metasurfaces," *Appl. Comput. Electromagn. Soc. J.*, vol. 29, no. 12, pp. 960–976, 2014.

[72] F. Costa, S. Genovesi, A. Monorchio, and G. Manara, "A circuit-based model for the interpretation of perfect metamaterial absorbers," *IEEE Trans. Antennas Propag.*, vol. 61, no. 3, pp. 1201–1209, 2013.

[73] S. Baco, A. Chik, and F. Md. Yassin, "Study on Optical Properties of Tin Oxide

Thin Film at Different Annealing Temperature," *J. Sci. Technol.*, vol. 4, pp. 61–72, 2012.

[74] J. Isidorsson, C. G. Granqvist, K. von Rottkay, and M. Rubin, "Ellipsometry on sputter-deposited tin oxide films: optical constants versus stoichiometry, hydrogen content, and amount of electrochemically intercalated lithium.," *Appl. Opt.*, vol. 37, no. 31, pp. 7334–7341, 1998.

[75] N. Kim, S. In, D. Lee, J. Rhie, J. Jeong, D. S. Kim, and N. Park, "Colossal Terahertz Field Enhancement Using Split-Ring Resonators with a Sub-10 nm Gap," *ACS Photonics*, vol. 5, no. 2, pp. 278–283, 2018.

[76] H. R. Park, X. Chen, N. C. Nguyen, J. Peraire, and S. H. Oh, "Nanogap-enhanced terahertz sensing of 1 nm thick (λ/106) dielectric films," *ACS Photonics*, vol. 2, no. 3, pp. 417–424, 2015.

[77] S. A. Kuznetsov, M. Navarro-Cía, V. V. Kubarev, A. V. Gelfand, M. Beruete, I. Campillo, and M. Sorolla, "Regular and anomalous extraordinary optical transmission at the THz-gap," *Opt. Express*, vol. 17, no. 14, pp. 11730–11738, Jul. 2009.

[78] V. Lomakin and E. Michielssen, "Enhanced transmission through metallic plates perforated by arrays of subwavelength holes and sandwiched between dielectric slabs," *Phys. Rev. B*, vol. 71, no. 23, p. 235117, Jun. 2005.

Author Merits

Journal Papers

- I. Jáuregui-López, P. Rodríguez-Ulibarri, A. Urrutia, S. A. Kuznetsov, and M. Beruete, "Labyrinth Metasurface Absorber for Ultra-High-Sensitivity Terahertz Thin Film Sensing," *Phys. status solidi - Rapid Res. Lett.*, vol. 1800375, pp. 1–7, 2018 (2018).

- I. Jáuregui-López, P. Rodríguez-Ulibarri, S. A. Kuznetsov, and M. Beruete, " THz Sensing With Anomalous Extraordinary Optical Transmission Hole Arrays" – **In preparation**.

International Conferences

- P. Rodriguez-Ulibarri, I. Jáuregui, M. Beruete, " Non-Bianisotropic Complementary Split Ring Resonators Metasurfaces", The 11th International Congress on Advanced Electromagnetic Materials in Microwaves and Optics, Metamaterials 2017 (2017).

- I. Jáuregui, P. Rodriguez-Ulibarri, S. A. Kuznetsov, M. Beruete, "THz sensing with classical FSS", The 10th International Congress on Advanced Electromagnetic Materials in Microwaves and Optics, Metamaterials 2016 (2016).

National Conferences

- P. Rodríguez-Ulibarri., I. Jáuregui, and M. Beruete, "Metasuperficies basadas en anillos complementarios sin bianisotropía," submitted to XXXII Symposium Nacional de la Unión Científica Nacional de Radio, URSI 2017, (2017).

- P. Roriguez-Ulibarri, I. Jáuregui, S. A. Kuznetsov, M. Beruete, "THz sensing structures based on classical cross-dipole FSS", XXXI Simposium Nacional de la Unión Científica Internacional de Radio, URSI 2016, (2016).

Research Projects Participation

- "Metasensores en el infrarrojo extendido – Metasensores de película delgada en THZ/MIR para aplicaciones agroalimentarias". Proyectos propios UPNA 2018.

- Yeast detection by infrared spectroscopy (YEDIS)" (0011-1365-2016-00008). Convocatoria:2016 (Gobierno de Navarra).

- "Sensores de terahercios e infrarrojo medio basados en metasuperficies funcionales para aplicaciones agroalimentarias y de seguridad alimentaria" (2016/pi014/METASUPERFICIE). Convocatoria: i+D 2016 (Gobierno de Navarra).

- "Componentes inspirados en metamateriales para sensado avanzado desde los terahercios hasta el óptico: sensores en terahercios" (TEC2014-51902-C2-2-R). Convocatoria: Plan Estatal 2014.

- "Early invasive fungal infection detection with Terahertz sensor systems" (IIS14618.RI1). Convocatoria: Eurotransbio 2012.

Awards

- Premios Liberalización de las Telecomunicaciones 2016 (COGITT/AEGITT).